Icarus 197 (2008) 321–347

Contents lists available at ScienceDirect

Icarus

www.elsevier.com/locate/icarus

Ultraviolet spectral reflectance properties of common planetary minerals

Edward A. Cloutis [a,*], Kaitlyn A. McCormack [a], James F. Bell III [b], Amanda R. Hendrix [c], Daniel T. Bailey [a], Michael A. Craig [a,1], Stanley A. Mertzman [d], Mark S. Robinson [e], Miriam A. Riner [e,2]

[a] Department of Geography, University of Winnipeg, 515 Portage Avenue, Winnipeg, MB, R3B 2E9, Canada
[b] Department of Astronomy, Cornell University, 402 Space Sciences Building, Ithaca, NY 14853-6801, USA
[c] Jet Propulsion Laboratory, 4800 Oak Grove Drive, Pasadena, CA 91109, USA
[d] Department of Earth and Environment, Franklin and Marshall College, Lancaster, PA 17604-3003, USA
[e] School of Earth and Space Exploration, Arizona State University, Tempe, AZ 85287-1404, USA

ARTICLE INFO

Article history:
Received 17 December 2007
Revised 16 April 2008
Available online 20 May 2008

Keywords:
Ultraviolet observations
Spectroscopy
Moon, surface
Spectroscopy
Mars, surface

ABSTRACT

Ultraviolet spectral reflectance properties (200–400 nm) of a large number of minerals known or presumed to exist on the surfaces of Mars, the Moon, and asteroids, and in many meteorites, were investigated. Ultraviolet reflectance spectra (200–400 nm) of these minerals range from slightly blue-sloped (reflectance decreasing toward longer wavelengths) to strongly red-sloped (reflectance increasing toward longer wavelengths). Most exhibit one or two absorption features that are attributable to Fe–O charge transfers involving Fe^{3+} or Fe^{2+}. The UV region is a very sensitive indicator of the presence of even trace amounts (<0.01 wt%) of Fe^{3+} and Fe^{2+}. The major Fe^{3+}–O absorption band occurs at shorter wavelengths (~210–230 nm), and is more intense than the major Fe^{2+}–O absorption band (~250–270 nm). Ti-bearing minerals, such as ilmenite, rutile and anatase exhibit UV absorption bands attributable to Ti^{4+}–O charge transfers. While the positions of metal–O charge transfer bands sometimes differ for different minerals, the variation is often not diagnostic enough to permit unique mineral identification. However, iron oxides and oxyhydroxides can generally be distinguished from Fe-bearing silicates in the 200–400 nm region on the basis of absorption band positions. Within a given mineral group (e.g., low-calcium pyroxene, olivine, plagioclase feldspar), changes in Fe^{2+} or Fe^{3+} abundance do not appear to result in a measurable change in absorption band minima positions. Absorption band positions can vary as a function of grain size, however, and this variation is likely due to band saturation effects. The intensity of metal–O charge transfers means that some minerals will exhibit saturated UV absorption bands even for fine-grained (<45 μm) powders. In cases where absorption bands are not saturated (e.g., Fe^{2+}–O bands in some plagioclase feldspars and pyroxenes), changes in Fe^{2+} content do not appear to cause variations in band position. In other minerals (e.g., olivine), changes in band positions are correlated with compositional and/or grain size variations, but this is likely due to increasing band saturation rather than compositional variations. Overall, we find that the UV spectral region is sensitive to different mineral properties than longer wavelength regions, and thus offers the potential to provide complementary capabilities and unique opportunities for planetary remote sensing.

1. Introduction

The ultraviolet (UV) spectral region is one which has been largely underexploited for remote sensing of solid planetary surfaces. This arises largely from the fact that the Earth's atmosphere is relatively opaque below ~350 nm. Thus, space-based observations are required in order to fully utilize this wavelength region for planetary surface mapping. Indeed, recent observational studies have suggested that this wavelength region has some potential for geological mapping of Solar System bodies and may provide otherwise unobtainable geological, compositional, and/or physical properties information (e.g., Hendrix et al., 2003; Hendrix and Vilas, 2006; Robinson et al., 2007; Bell and Ansty, 2007).

The Moon was the first planetary target studied in the UV spectral region (here defined as the interval from 200 to 400 nm). Early studies include Zond-3 spacecraft measurements (Lebedinsky et al., 1967a, 1967b, 1968), rocket-based whole-disk images (Carver et al., 1974), and a number of other more restricted studies (e.g., Stair and Johnson, 1953; Lucke et al., 1973, 1976, and references therein). Asteroids were also surveyed at UV wavelengths and many show evidence for shallow absorption bands, spectral differences among various taxonomic classes, and "anomalous" UV

* Corresponding author. Fax: +1 204 774 4134.
E-mail address: e.cloutis@uwinnipeg.ca (E.A. Cloutis).
[1] Now at University of Western Ontario.
[2] Now at University of Hawaii.

0019-1035/$ – see front matter
doi:10.1016/j.icarus.2008.04.018

properties (e.g., Butterworth and Meadows, 1985). UV spectra of meteorites have also hinted at compositional information that may be obtained from this wavelength region (e.g., Dollfus et al., 1980; Wagner et al., 1987).

More recently, space-based telescopes have enabled high spatial resolution UV observations of planetary surfaces, including Hubble Space Telescope imaging of the Moon (Garvin et al., 2006; Robinson et al., 2006, 2007) and Europa (Noll et al., 1995). Recently deployed and upcoming planetary orbiters will be capable of conducting planetary surface observations in the UV, including LROC on the Lunar Reconnaissance Orbiter (300 and 360 nm imaging bands; Chin et al., 2007), SPICAM on Mars Express (118–320 nm; Bertaux et al., 2006), MARCI on the Mars Reconnaissance Orbiter (imaging bands at 260 and 320 nm; Malin, 2006), and the MESSENGER MASCS instrument (spectroscopy from 115 to 600 nm with ~1 nm resolution; Gold et al., 2001).

UV spectra of planetary surfaces are, in general, characterized by decreasing reflectance toward shorter wavelengths, with few, if any, well-defined absorption bands. For example, in Mariner 9 ultraviolet observations of Mars airborne dust, Pang et al. (1982) detected spectral features near 210, 250, and 300 nm that they assigned to Ti–O charge transfers in the anatase polymorph of TiO_2. This assignment was bolstered by the detection of Ti by the Viking landers and the lack of other spectral analogues for these features. Space weathering of asteroids and the Moon may also manifest itself in the UV region (e.g., Shkuratov et al., 1985; Hendrix and Vilas, 2006), and the UV may be a more sensitive indicator of space weathering than longer wavelength regions (Hendrix and Vilas, 2006; Vilas and Hendrix, 2006). Carlson et al. (1999) and Hendrix et al. (1998, 2003) detected hydrogen peroxide on Europa and Ganymede and hemispheric asymmetries on Europa using Galileo spectra, partially on the basis of spectral behavior in the 200–300 nm interval. Recent HST observations of the Moon (Garvin et al., 2006; Robinson et al., 2007) suggest that unique compositional information may be derivable from UV observations. Much of this information relates to the presumed UV spectral uniqueness of ilmenite compared to other common lunar minerals, and thus the UV region may be useful for determination of ilmenite abundance.

Analysis of observational UV data has been largely hampered by the lack of systematic spectral-compositional laboratory spectroscopic data for minerals known or presumed to exist on various Solar System bodies. The vast majority of previous laboratory studies that have been undertaken either have included only a limited range of samples and/or are not accompanied by compositional information from which correlations between spectral variations and composition or structure can be derived. The availability of high-quality laboratory spectra of planetary materials has also been hampered by a number of technical issues, including low UV intensities for most illumination sources, the unavailability of suitable spectrometers capable of reproducing planetary observing conditions (e.g., broadband target illumination coupled with wavelength selective detectors), generally low UV sensitivity for the most common types of detectors, and a lack of suitable reflectance standards.

In addition to planetary mapping, knowledge of the UV spectral properties of geologically significant minerals may also enable better modeling of heat flow in the interiors of the Earth and other planets. For example, the significance and magnitude of heat transport in the Earth's mantle through radiative heat transport is strongly dependent on the spectral properties (transparency, opacity) of mantle materials as a function of wavelength. These properties are very sensitive to factors such as grain size, temperature, structure, composition, and Fe oxidation state and electron spin configuration (e.g., Shankland et al., 1979; Smith and Langer, 1982; Badro et al., 2004; Hofmeister, 2005).

With the increasing evidence that UV spectral measurements of planetary surfaces may be able to provide geological information that is unique or complementary to that derivable from longer wavelength observations, we initiated a comprehensive laboratory-based investigation of the UV spectral reflectance properties of a wide range of geologically-important materials, coupled to comprehensive compositional and structural data for these samples. Our approach is designed to enable more detailed and quantitative interpretation of planetary UV observations.

2. Previous UV laboratory observations

As mentioned above, previous laboratory-based UV spectral reflectance studies of geological materials generally have been limited in terms of number of samples, accompanying sample information, spectral resolution, or wavelength coverage. For completeness, and as a baseline against which our new study can be compared, the results of many of these previous studies, and the experimental procedures they employed, are provided in Appendix A.

3. Experimental conditions of previous studies

Most of the previous studies discussed in Appendix A provided useful information on the UV properties of minerals. However, a number suffer from various shortcomings that limit their utility for quantitative analysis of UV observational data. These limitations are both technical and procedural. They include: the reliability/linearity of the detector systems; the use of a monochromatic illumination source and broadband detector; the absolute reflectance of the standards used for the measurements; and an inability to derive absolute reflectance. A review of these previous studies is provided in Appendix B.

4. Experimental procedure of this study

A diverse suite of samples was included in this study (Table 1). The selected samples were designed to largely encom-

Table 1a
Composition of samples used in this study

	Meteoritic metal		Hematites			Goethite	Magnetite
wt%	MET100	wt%	HEM101	HEM102	HEM103	OOH003	MAG103
Fe	93.39	SiO_2	1.06	0.29	0.31	1.02	0.00
Ni	6.07	Al_2O_3	0.39	0.71	0.71	0.47	0.43
Na	0.00	FeO	0.19	0.91	1.33	0.43	28.80
S	0.00	Fe_2O_3	97.40	96.66	96.35	96.17	60.38
V	0.00	MgO	0.14	0.36	0.35	0.89	tr.
Co	0.50	CaO	0.06	0.13	0.05	0.07	0.00
P	0.02	Na_2O		0.29	0.28	0.00	0.00
Cr	0.18	TiO_2	0.03	0.02	0.03	0.04	7.28
Mg	0.00	Cr_2O_3		tr.	tr.	tr.	tr.
Mn	0.00	V_2O_5		0.01	0.08	tr.	0.05
Cu	0.00	CoO		0.08	0.08		
Al	0.03	ZnO					0.42
Pb	0.87	NiO		0.00	0.00		tr.
Zn	0.11	MnO	0.00	0.01	0.02	0.23	2.00
Ti	0.00	SrO				tr.	
		P_2O_5	0.00	0.04	0.02	0.61	
		K_2O	0.00	0.01	0.01	0.02	
		SO_3	0.25	0.32	0.40		
		ZrO_2				tr.	
		H_2O	0.56				
		LOI				10.36	
Total	101.17	Total	100.08	99.85	100.02	99.95[a]	99.36

Abbreviations: tr.: <0.01 wt%; LOI: loss on ignition up to 950 °C.
Source of samples: MET100: Odessa, Texas iron meteorite; HEM101: synthetic sample from Dick Morris; HEM102: Souse, AZ, USA; HEM103: unknown locality; OOH003: Cary Mine, Ironwood, Gogebic Co., MI, USA; MAG103: Langesundfjord, Norway.
[a] Total expressed on a volatile-free basis.

Table 1b

	Ilmenites			Palagonitic soils	
wt%	ILM101	ILM102	ILM103	PAL101	PAL102
SiO_2	0.40	0.61	0.09	41.28	47.19
Al_2O_3	0.72	0.94	0.28	26.02	21.95
FeO	1.38	24.64	31.60	2.59	2.67
Fe_2O_3	33.05	18.61	1.32	13.00	11.73
MgO	0.43	2.72	0.43	3.26	3.12
CaO	0.15	0.32	0.07	4.64	5.13
Na_2O	0.41	0.61	0.39	2.50	2.21
TiO_2	63.28	50.69	64.20	3.77	3.47
Cr_2O_3	tr.	0.05	tr.	tr.	tr.
V_2O_5	0.07	0.16	tr.	0.01	0.01
CoO	tr.	0.05	tr.		
MnO	0.01	0.12	1.19	0.30	0.24
SrO			tr.	0.10	0.14
P_2O_5	0.03	0.12	0.03	1.52	0.61
K_2O	0.01	0.08	0.03	0.65	0.98
ZrO_2				0.08	0.06
LOI				15.45	10.30
Total	99.94	99.72	99.63	100.39[a]	100.58[a]

Abbreviations: tr.: <0.01 wt%; LOI: loss on ignition up to 950 °C.
Source of samples: ILM101: Krageroo, Telemark, Norway; ILM102: St. Urbain, QC, Canada; ILM103: Old Mica Mine, Saluda Co., SC, USA; PAL101: Mauna Kea, HI, USA; PAL102: Mauna Kea, HI, USA.
[a] Total expressed on a volatile-free basis.

Table 1c

	Olivines						
wt% NMNH#	OLV002	OLV003	OLV007	OLV008	OLV011 35117	OLV022	OLV103
SiO_2	39.74	40.64	41.72	36.65	29.78	36.50	39.58
FeO	12.62	9.25	2.71	7.15	61.46	28.52	10.14
Fe_2O_3	1.43	0.59	0.45	0.00	5.52	8.64	6.31
MgO	46.38	49.13	54.65	51.19	0.05	27.73	44.59
MnO	0.23	0.09	0.19	2.15	2.14		0.18
ZnO	0.00	0.00	0.00	0.11	0.54		0.00
NiO	0.32	0.33	0.01	0.03	0.04	0.12	0.40
CaO	0.13	0.07	0.63	tr.	0.05	0.01	0.00
TiO_2	tr.	0.00	0.00	0.01	tr.		0.00
Cr_2O_3	tr.	0.01	tr.	0.00	0.00		tr.
CoO	0.06	0.04	0.01	0.02	0.10		0.06
V_2O_5	0.00	0.00	0.00	tr.	0.00		0.00
K_2O	0.00	0.00	0.00	0.00	0.00		0.00
Na_2O	0.00	0.00	0.00	0.00	0.00		0.00
Al_2O_3	0.00	0.00	0.00	0.00	0.00	0.09	0.00
Total	100.91	100.15	100.37	97.31	99.68	101.61	101.26
Fo	86.7	90.4	97.3	92.7	0.1	63.4	88.7
Fa	13.3	9.6	2.7	7.3	99.9	36.6	11.3

Abbreviations: MNMH#: ID number of samples from the Smithsonian Institution National Museum of Natural History; tr.: <0.01 wt%; Fo: mol% forsterite; Fa: mol% fayalite.
Source of samples: OLV002: xenolith in basalt, cinder cone, Hale Pohaku, HI, USA; OLV003: Peridot, San Carlos Co., AZ, USA; OLV007: Palumbo Farm, Villafranca, Cecchina, near Rome, Italy; OLV008: Kafveltorp Quarry, near Kopperberg, Sweden; OLV011: Rockport, MA, USA; OLV022: Skaergaard intrusion, Greenland; OLV103: Loch Seaforth, Outer Hebrides, Scotland.

pass the major mineral species known to occur on the Moon and Mars, but also to include minerals of asteroidal and meteoritic relevance. The sample suite encompasses meteoritic metal, eleven oxides/hydroxides (three hematites, goethite, magnetite, two TiO_2 polymorphs, and four ilmenites), seven olivines, twelve plagioclase feldspars, eight low-calcium pyroxenes, fourteen high-calcium pyroxenes (seven each of spectral type A and B; Adams, 1974), one basalt, two palagonitic soils, three sulfates, and three phyllosilicates.

The samples were prepared for spectral measurements by both wet sieving with acetone (the <45-μm fractions of the olivines, pyroxenes, and plagioclase feldspars) and dry sieving (the remaining samples). The powders were prepared by crushing the samples

Table 1d

	Pyroxenes						
wt%	PYX003	PYX005	PYX009	PYX010	PYX017	PYX018	PYX020
SiO_2	50.33	49.70	53.90	51.94	50.57	55.17	55.23
Al_2O_3	5.46	4.12	0.51	0.50	4.09	0.37	0.59
FeO	17.30	5.93	6.20	10.18	4.88	2.42	2.07
Fe_2O_3	1.43	0.77	0.00	4.83	1.25	0.00	0.00
MgO	23.58	13.80	14.18	9.31	16.05	17.01	17.06
CaO	1.59	22.94	25.08	21.65	20.85	23.93	24.08
Na_2O	0.05	0.57	0.05	1.39	0.32	0.51	0.52
TiO_2	0.41	1.48	0.01	tr.	1.04	tr.	0.09
Cr_2O_3	0.11	0.17	0.04	0.03	0.78	0.91	0.96
V_2O_5	0.02	0.00	0.02	tr.	0.02	0.03	0.05
CoO	0.04	0.04	0.05	0.02	0.03	0.02	0.05
NiO	0.01	0.04	0.15	0.01	0.06	0.07	0.06
MnO	0.29	0.11	0.26	0.52	0.13	0.10	0.10
Total	100.62	99.67	100.45	100.38	100.07	100.54	100.86
En	68.5	41.0	39.8	30.4	47.5	47.8	48.0
Fs	28.2	9.9	9.7	18.7	8.1	3.8	3.3
Wo	3.3	49.1	50.5	50.9	44.4	48.4	48.7
∑M2	0.072	0.967	1.007	1.004	0.871	0.994	0.999

Abbreviations: tr.: <0.01 wt%; En: mol% enstatite; Fs: mol% ferrosilite; Wo: mol% wollastonite; ∑M2: sum of M2 site-preferring cations (Cr + Ca + Co + Mn + Na + Zn).
Source of samples: PYX003: Mantyharja, Finland; PYX005: unknown locality; PYX009: Canada; PYX010: unknown locality; PYX017: Tillamook burn area, near Grindstone Lookout, Tillamook Co., OR, USA; PYX018: near Dallas Gem Mine, San Benito Co., CA, USA; PYX020: Hirado Mine, Hirado-Mura, Bugi-Gun, Gifu-ken, Honshu, Japan.

Table 1e

	Pyroxenes							
wt% NMNH	PYX021	PYX023	PYX032	PYX034	PYX036	PYX038	PYX039 R15398	PYX042
SiO_2	48.35	56.86	50.21	49.80	50.54	49.40	51.45	56.59
Al_2O_3	0.54	0.76	1.24	5.63	2.99	0.31	1.16	0.09
FeO	23.25	6.36	23.65	5.21	8.18	17.49	10.26	8.93
Fe_2O_3	3.81	0.83	5.11	2.03	1.71	8.70	6.47	0.84
MgO	1.25	34.04	17.57	14.58	14.64	3.06	8.47	33.88
CaO	21.66	0.65	1.59	19.86	20.35	20.80	20.03	0.22
Na_2O	0.18	0.00	0.00	1.06	0.27	0.61	2.14	0.00
TiO_2	0.00	0.01	0.19	1.55	0.86	0.00	0.05	0.04
Cr_2O_3	0.02	0.45	0.04	0.12	0.07	0.02	0.02	0.04
V_2O_5	tr.	tr.	tr.	0.01	0.08	0.00	tr.	tr.
CoO	0.05	0.03	0.06	0.03	0.04	0.08	0.05	0.02
NiO	0.02	0.08	0.01	0.05	0.02	0.01	0.02	0.01
MnO	1.17	0.17	0.53	0.12	0.25	0.61	0.67	0.04
Total	100.31	100.24	100.20	100.05	100.00	101.09	100.79	100.70
En	4.2	89.3	54.9	47.4	43.3	11.0	29.6	86.8
Fs	43.7	9.4	41.5	8.9	13.4	35.2	20.1	12.8
Wo	52.1	1.3	3.6	43.7	43.3	53.8	50.3	0.4
∑M2	0.999	0.042	0.085	0.857	0.846	0.951	0.998	0.011

Abbreviations: MNMH#: ID number of samples from the Smithsonian Institution National Museum of Natural History; tr.: <0.01 wt%; En: mol% enstatite; Fs: mol% ferrosilite; Wo: mol% wollastonite; ∑M2: sum of M2 site-preferring cations (Cr + Ca + Co + Mn + Na + Zn).
Source of samples: PYX021: Rio Marina, Elba, Italy; PYX023: Mirabel Springs, Mt. St. Helena, Lake Co., CA, USA; PYX032: Ekersund, Norway; PYX034: Hopi Buttes, Winslow, AZ, USA; PYX036: Buffaure, Val di Fassa, Trento, Italy; PYX038: Avery Co., NC, USA; PYX039: Risor, Aust-Adger, Norway; PYX042: Bamle, Norway.

in an alumina mortar and pestle and removing impurities through a combination of hand picking under a binocular microscope and separation with a hand magnet during crushing and sieving. Dry sieving was performed by gently brushing the crushed samples in the 45-μm sieve to dislodge adhering finer-grained particles. For wet sieving, the powders were repeatedly rinsed in acetone while in the 45-μm sieve. For determining the effects of grain size on UV spectral properties, samples in the size ranges <45, 45–90, 90–250, 250–500, and 500–1000 μm were prepared for ilmenite, hematite, olivine, plagioclase feldspar, and low-calcium pyroxene.

Table 1f

	Pyroxenes						
wt%	PYX101	PYX108	PYX110	PYX114	PYX117	PYX119	PYX150
SiO_2	50.63	56.97	56.65	51.27	53.54	55.40	55.75
Al_2O_3	1.49	0.82	0.03	1.91	1.54	1.31	0.24
FeO	12.99	5.29	9.19	11.34	16.17	9.92	2.56
Fe_2O_3	1.44	1.13	0.44	0.57	1.02	0.72	0.00
MgO	11.52	34.82	33.92	14.47	27.53	32.37	16.26
CaO	19.99	0.54	0.30	18.45	0.35	0.19	25.70
Na_2O	0.16	0.00	0.00	0.23	0.00	0.00	0.05
TiO_2	0.67	0.02	0.03	0.95	0.03	0.04	0.00
Cr_2O_3	0.14	0.38	0.05	0.17	0.07	0.68	tr.
V_2O_5	0.05	0.00	0.01	0.04	0.00	0.00	0.00
CoO	0.05	0.02	0.01	0.04	0.01	0.03	0.05
NiO	0.09	0.05	0.02	0.04	0.05	0.05	tr.
MnO	0.38	0.18	0.04	0.28	0.44	0.26	0.11
Total	99.60	100.22	100.69	99.76	100.75	100.97	100.75
En	34.7	91.1	86.3	41.1	74.7	85.1	44.9
Fs	22.0	7.8	13.2	19.1	24.6	14.6	4.0
Wo	43.3	1.1	0.5	39.8	0.7	0.3	51.1
∑M2	0.849	0.037	0.013	0.778	0.029	0.035	1.003

Abbreviations: tr.: <0.01 wt%; En: mol% enstatite; Fs: mol% ferrosilite; Wo: mol% wollastonite; ∑M2: sum of M2 site-preferring cations (Cr + Ca + Co + Mn + Na + Zn).
Source of samples: PYX101: Loudon Co., VA, USA; PYX108: Jackson Co., NC, USA; PYX110: unknown locality; PYX114: Skaergaard intrusion, Greenland; PYX117: India; PYX119: Loch Seaforth, Harris, Outer Hebrides, Scotland; PYX150: unknown locality.

Table 1g

	Plagioclase feldspars					
wt%	PLG103	PLG104	PLG105	PLG106	PLG108	PLG109
SiO_2	69.08	54.90	58.73	65.89	46.55	50.77
Al_2O_3	19.16	27.85	24.99	21.21	32.70	31.19
Na_2O	11.79	5.21	7.33	10.51	1.71	3.60
CaO	0.01	11.05	7.95	2.08	17.28	13.71
K_2O	0.03	0.37	0.05	0.09	0.02	0.12
SrO	0.04	0.10	0.04	0.21	0.03	0.08
BaO	tr.	0.06	0.06	0.07	0.03	0.04
Fe_2O_3[a]	0.03	0.41	0.07	0.07	0.64	0.43
TiO_2	0.02	0.06	0.02	0.02	0.05	0.03
NiO	0.04	0.05	0.05	0.04	0.09	0.07
MnO	0.01	0.01	0.01	0.01	0.01	tr.
Cr_2O_3	0.03	0.04	0.00	0.03	0.03	0.05
CoO	0.03	0.03	0.01	0.01	0.03	0.03
V_2O_5	0.02	0.01	tr.	tr.	0.01	0.01
MgO	0.00	0.07	0.00	0.00	0.04	0.02
ZnO	0.01	0.01	tr.	tr.	0.02	0.02
Total	100.30	100.23	99.31	100.24	99.24	100.17
Ab	99.8	45.1	62.3	89.7	15.2	32.0
An	0.1	52.8	37.4	9.8	84.7	67.3
Or	0.1	2.1	0.3	0.5	0.1	0.7

Abbreviations: tr.: <0.01 wt%; Ab: mol% albite; An: mol% anorthite; Or: mol% orthoclase.
Source of samples: PLG103: Bob Ingersoll Mine, Keystone, Pennington Co., SD, USA; PLG104: Nain, NL, Canada; PLG105: Sannidal, Norway; PLG106: Dungannon Township. ON, Canada; PLG108: Stillwater complex, MT, USA; PLG109: unknown locality.
[a] All Fe reported as Fe_2O_3.

Table 1h

	Plagioclase feldspars					
wt%	PLG111	PLG114	PLG115	PLG120	PLG122	PLG130
SiO_2	48.60	43.97	62.07	65.28	44.80	49.20
Al_2O_3	33.52	34.66	23.58	21.94	35.05	31.74
Na_2O	2.32	0.65	8.98	9.89	0.81	2.60
CaO	15.46	19.03	4.99	3.10	18.76	15.56
K_2O	0.01	0.00	0.03	0.40	0.00	0.06
SrO	0.07	0.06	0.28	0.06	0.08	n.d.
BaO	0.03	0.05	0.03	0.01	0.05	n.d.
Fe_2O_3[a]	0.59	0.58	0.07	0.14	0.61	0.42
TiO_2	0.06	0.05	0.02	0.03	0.05	0.04
NiO	0.10	0.08	0.05	0.05	0.08	0.00
MnO	0.00	0.01	0.01	tr.	0.01	0.01
Cr_2O_3	0.00	0.03	0.02	0.03	0.02	0.00
CoO	0.03	0.04	0.01	0.01	0.04	0.00
V_2O_5	0.01	0.02	tr.	tr.	0.01	0.00
MgO	0.14	0.01	0.03	0.00	0.01	0.26
ZnO	0.00	0.03	tr.	0.00	0.03	0.00
Total	100.94	99.27	100.17	100.94	100.41	99.92
Ab	21.3	5.8	76.4	83.5	7.2	23.1
An	78.6	94.2	23.5	14.4	92.8	76.5
Or	0.1	0.0	0.1	2.1	0.0	0.4

Abbreviations: n.d.: not determined; tr.: <0.01 wt%; Ab: mol% albite; An: mol% anorthite; Or: mol% orthoclase.
Source of samples: PLG111: locality unknown; PLG114: locality unknown; PLG115: Carter Mine, Holcomb Ranch, Madison Co., NC, USA; PLG120: near Crown Point, Essex Co., NY, USA; PLG122: Grass Valley, Nevada Co., CA, USA; PLG130: Split Rock, MN, USA.
[a] All Fe reported as Fe_2O_3.

Table 1i

	Basalt	Phyllosilicates			Sulfates		
wt% NMNH#	SA-51	CHM102 R4558	MON101	NON101	SPT107	SPT143	SPT207
SiO_2	48.47	21.77	65.85	61.40	0.02	0.00	0.71
Al_2O_3	12.33	5.62	19.89	9.49	0.00	0.06	0.51
FeO	9.42	29.09	0.26	0.79	0.16	0.00	0.52
Fe_2O_3	7.79	25.92	5.65	22.08	89.76	0.00	0.22
MgO	4.29	4.06	2.02	1.07	0.18	25.09	0.47
CaO	7.50	6.36	0.94	0.10	0.22	0.46	97.33
Na_2O	2.12	0.77	1.30	0.15	6.79	0.94	0.15
TiO_2	4.15	0.23	0.67	0.38	0.00	0.00	0.01
Cr_2O_3	0.04	0.04	tr.	tr.	tr.		
V_2O_5	0.06	0.07	0.01	0.01	0.01		tr.
NiO					0.00		
MnO	0.25	0.51	0.02	0.03	0.02	0.01	0.00
P_2O_5	0.88	1.71	0.04	0.51	0.04	0.04	0.03
K_2O	1.51	0.06	2.90	3.67	2.15	0.09	0.04
SrO	0.10						0.28
ZrO_2	0.08						0.01
SO_3					27.87		46.31
LOI[a]	15.45	20.87	10.38	8.56	31.63	38.11	20.91
Total	98.99[b]	99.34	99.57	99.76	99.38[b]	26.69[b]	100.28[b]

Abbreviations: MNMH#: ID number of samples from the Smithsonian Institution National Museum of Natural History; tr.: <0.01 wt%.
Source of samples: SA-51: Roza Dike, Columbia River basalt, Wallowa Co. OR, USA; CHM102: Chamois, France; MON101: Cameron, AZ, USA; NON101: Allentown, Lehigh Co., PA, USA; SPT107: Skouriotissa mine, Cyprus; SPT143: Basque Lakes, near Ashcroft, BC, Canada; SPT207: Gypsumville, MB, Canada.
[a] LOI: weight loss upon heating sample in air to 950 °C.
[b] Total expressed on an LOI-free basis.

The natural samples were all characterized by a combination of electron microprobe analysis, wet chemistry (for Fe^{2+}/Fe^{3+} ratios), and X-ray diffraction. Details of these procedures can be found in Cloutis et al. (1990), Cloutis and Gaffey (1991), Mertzman (2000), and Cloutis and Bell (2004). The compositions of the samples are provided in Table 1. One ilmenite (ILM200) and the two TiO_2 polymorphs (PIG007 and PIG008) are synthetic samples purchased from Sigma–Aldrich and were not independently characterized.

As discussed above, acquisition of UV reflectance spectra is difficult due to a number of factors, including low incident light levels from most illumination sources, generally low detector sensitivity and increasing atmospheric absorption toward shorter wavelengths, and lack of a reliable UV reflectance standard. Our adopted experimental procedure attempted to minimize the effects of all of these potential difficulties.

The instrument used for the spectral measurements was an Ocean Optics S-2000 spectrometer equipped with a grating that provides coverage from 200 to 859 nm with spectral resolution between 0.36 nm (at 200 nm) and 0.28 nm (at 859 nm). Illumination was provided by an Analytical Instrument Systems Inc.

Mini-DTA light source which utilizes a 50-W deuterium lamp. After experimenting with multiple configurations we found that the best compromise between integration time and signal-to-noise ratio was provided by delivering the illumination through a bifurcated fiber optic bundle consisting of six illumination fibers surrounding a central pick-up fiber feeding into the detector array. This assembly consisted of 400-μm diameter solarization-resistant (XSR) fibers, with transmission efficiencies between 23 and 40% across the 200–400 nm range. The fiber optic bundle was used in normal incidence and we used an integration time of 500 ms and averaged 900 individual spectra. Extensive tests of our instrument also showed that, for our particular spectrometer, we could saturate the detector outside of our wavelength range of interest and not affect the spectra in the 200–400 nm range. This allowed us to increase integration times by a factor of ∼10 over the time that would have been required to avoid detector saturation. This resulted in a measurement time of ∼8 min per standard, sample, or dark current. Measurements for each sample were made by first acquiring a dark current spectrum (with the input to the spectrometer blocked), a reference spectrum of our $BaSO_4$ standard (see below), followed by measurement of the sample. All three measurements were made using an identical viewing geometry, integration time, and number of averaged spectra. The reference and target were both placed at the same distance from the end of the fiber bundle (5 mm). The fibers have a 25° field of view, and this working distance provided the best compromise between measurement time, uniform target illumination, and size of the sample being imaged. The most appropriate definition of the set-up is a biconical arrangement with i and e centered on ∼0° and detector and illumination fields of view of ∼25°.

The lack of a well-calibrated and/or uniform powdered reflectance standard was, and remains, an issue of concern. While many potential reflectance standards are known and have been calibrated to as low as ∼250 nm, there was a general lack of information on the optical properties of materials between 200 and 250 nm. In addition, there were concerns about differences between the way reflectance standards are calibrated versus the way we proposed to conduct our spectral measurements. The results of Saunders and Ott (1976) concerning fluorescence of halon being significant depending on how spectral measurements are conducted were instructive in this regard. We evaluated a wide variety of materials as potential reflectance standards, including halon, Spectralon, $BaSO_4$, MgF_2, BaF_2, CaF_2, pure Al powder, steel plates, and roughened Al sheets. The fluoride compounds were examined because they are widely utilized in UV photolithography. We found that all these materials exhibited downturns in reflectance below ∼250 nm. Deviations from constant reflectance were evaluated by comparing bidirectional ($i = 30°$, $e = 0°$) reflectance of these potential standards to the light directed directly at the detector.

We settled on $BaSO_4$ as an intermediate reflectance standard because of its stability and other beneficial properties as discussed above. We used a synthetic high-purity $BaSO_4$ powder (Alfa Aesar Puratronic grade: 99.998% metals basis; CAS #7727-43-7). This material was placed in an Al sample holder with a central bore 20 mm wide and 10 mm deep. These dimensions ensured that essentially no light interacted with the sample holder. The powder was gently tamped into the sample holder and a flat diffuse surface was achieved by tapping the sample holder, "chopping" the powder with the edge of a glass slide to fill in surface irregularities, and drawing the edge of the glass slide across the powder in a sawing motion to provide a final matte surface.

This arrangement provided excellent repeatability but did not provide absolute reflectance data. This is due to the fact that $BaSO_4$ is known to have spectral features below 400 nm (Grum and Luckey, 1968; Grum and Saltzman, 1976; Hapke and Wells, 1981), and its spectral behavior below 250 nm is poorly constrained. To correct for the deviations of $BaSO_4$ from ideal reflectance we utilized a precision DUV-enhanced mirror from Edmund Optics. This mirror has reflectance between 86% at 200 nm and 90% at 390 nm at normal incidence. The "absolute" reflectance of our $BaSO_4$ standard as measured against the DUV mirror, is very similar in shape to that measured by Hapke and Wells (1981), exhibiting a broad weak absorption band centered near 320 nm and a decrease in reflectance below ∼260 nm. The reality of an apparent upturn in reflectance shortward of ∼210 nm seen in our $BaSO_4$ spectrum could not be independently confirmed. The overall shape of the $BaSO_4$ standard was also consistent with the measurements where no optical fibers were used, and the deuterium light was shone directly onto the spectrometer as the standard, and set at 90° viewing geometry for measurement of the $BaSO_4$ reflectance (Fig. 1).

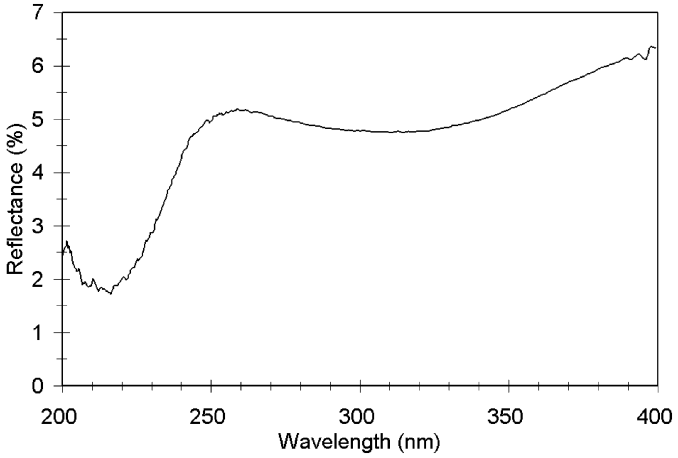

Fig. 1. Reflectance spectrum of $BaSO_4$ relative to UV mirror used to correct spectra for deviations from ideal reflectance for $BaSO_4$.

Deuterium lamps do not provide a smooth spectral output but include a number of emission features of variable intensity, particularly near 205, 211, 238, 255, and 400 nm. These emission lines proved useful for ensuring that the working distance for the sample and standard was maintained throughout the experiment. However, it was also found that the most intense deuterium features, in the 205, 211, and 390–400 nm regions, were present in the $BaSO_4$ spectra when measured against the DUV mirror (see below) and when no fiber optics were used and the incident light was directed at the spectrometer and with a 90° viewing geometry for the $BaSO_4$. Our interpretation of this is that the light path is effectively different for $BaSO_4$ versus a mirror or directly through air because some of the light will scatter within the $BaSO_4$ before reaching the spectrometer, thereby effectively increasing its path length versus the standard mirror surface measurement. Consequently, spectral artifacts in the form of narrow ($\lesssim$3 nm wide) peaks and valleys appeared in the 200–212 and 390–400 nm regions.

The DUV mirror allowed us to correct the $BaSO_4$ spectrum for deviations from flat (ideal) reflectance. To determine absolute reflectance, we assumed that our $BaSO_4$ standard has 100% reflectance at 400 nm. This is within 1% of its actual value, and was checked against Spectralon and halon, and has been confirmed by other investigators (e.g., Commission Internationale de L'Eclairage, 1979; Hapke and Wells, 1981). Thus to derive absolute reflectance for our samples, we utilize the following equation:

$$\text{Absolute reflectance} = \frac{(\text{sample reflectance})}{(\text{BaSO}_4\ \text{reflectance})} \times \frac{(\text{normalized BaSO}_4)}{(\text{DUV mirror})}.$$

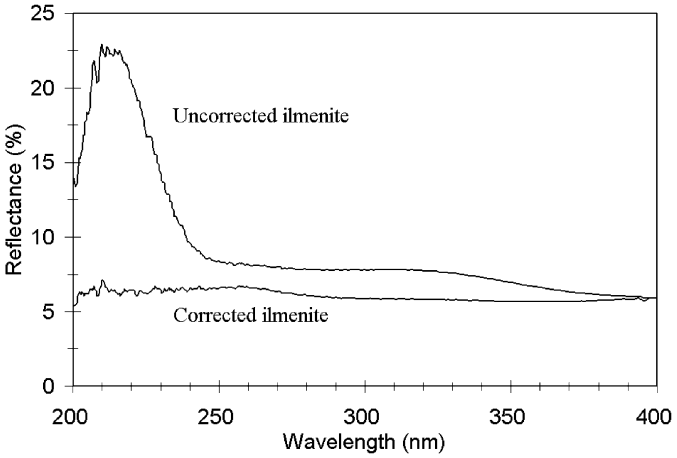

Fig. 2. Reflectance spectrum of ilmenite (ILM101, <45 μm) measured against $BaSO_4$ and corrected for deviations of $BaSO_4$ reflectance from ideality.

Dark current was subtracted from each term prior to calculating absolute reflectance. The effects that the assumption that $BaSO_4$ is a perfect diffuse reflector has on mineral spectra are shown in Fig. 2. It can be seen that the uncorrected data can show drastically different spectral shapes, particularly at shorter wavelengths. The artifacts introduced in the 390–400 nm region can also been seen in the corrected spectra. The corrected spectra have been posted to our web site: http://psf.uwinnipeg.ca.

In summary, the experimental procedure used in this study, and which provided the most reliable data, consisted of a UV-enhanced bifurcated fiber optic assembly with both illumination and detector fibers oriented normal to the sample, and a deuterium light source. A powdered $BaSO_4$ reflectance standard was used and was calibrated by both a DUV mirror and by shining the output of the lamp directly into the entrance aperture of the spectrometer.

5. Causes of UV absorption

The 200–400 nm spectra of most geological minerals are dominated by the intense metal–O charge transfer absorption that leads to generally decreasing reflectance toward shorter wavelengths, often with a local reflectance minimum in the 200–300 nm interval (e.g., Wagner et al., 1987). Few additional resolvable absorption bands are expected in this region for common rock-forming minerals (e.g., Burns, 1970, 1981; Cloutis, 2002). Most planetary targets also generally exhibit a decrease in reflectance toward shorter wavelengths (e.g., Lucke et al., 1973, 1976; Butterworth and Meadows, 1985; Calvin et al., 1995; Noll et al., 1995).

For common geological materials, the main cause of absorption in this wavelength is intense Fe–O charge transfer absorptions (e.g., Tossell, 1979), although other transition series elements also lead to metal–O charge transfer absorption bands in this region (McClure, 1962; Loeffler et al., 1974). In the case of lunar materials, it has been suggested that the Ti^{4+}–O charge transfer may be the greatest contributor to low reflectance in the UV (Tossell, 1979). Energy level calculations and experimental data provide information on where various metal–O charge transfer bands are expected (Table 2). Given the abundance of Fe and Ti relative to other transition series metals, our analysis has focused on these elements.

Both Fe^{3+} and Fe^{2+} can give rise to Fe–O charge transfer bands. Fe^{3+}–O charge transfer bands are generally two orders of magnitude stronger than Fe^{2+}–O bands (Soshea et al., 1958; Blazey, 1977). The wavelength position of Fe^{3+}–O transitions appears to be largely insensitive to metal–O distances (Sherman, 1983). In transmission spectra of Fe-doped MgO, two strong, resolvable Fe^{3+}–O bands are seen at 217 and 280 nm, as well as weaker bands near 312 and 394 nm, the latter of which is generally not well-resolved (Blazey, 1977). In general, Fe^{3+}–O charge transfers lead to a sharp rise in absorbance (decrease in reflectance) toward shorter wavelengths below ~500 nm, and this absorption edge moves to longer wavelengths with increasing Fe^{3+} content (Blazey, 1977; Smith, 1978; Keppler et al., 1994).

Table 2
Expected metal–O charge transfer absorption bands

Metal–O	Wavelength (nm)	Source of data
Octahedral Fe^{3+}	234, 280, 340, 395	1, 2
Non-octahedral Fe^{3+}	217	5
Tetrahedral Fe^{2+}	343	1, 2
Octahedral Fe^{2+}	267	1, 2
	<300	4
	250, 380	5
Octahedral Ti^{4+}	259, 296	1, 2
	250–300	3
Octahedral Ti^{3+}	216, 242	1, 2
Octahedral Cr^{3+}	169	1, 2
Octahedral V^{3+}	253, 303, 322	6
Octahedral Co^{3+}	~330	6
Octahedral Mn^{3+}	<200	6
Octahedral Ni^{2+}	<200	6

Source of data: 1: Loeffler et al. (1974); 2: Tossell et al. (1974); 3: Tossell (1979); 4: Strens and Wood (1979); 5: Blazey (1977); 6: McClure (1962).

Octahedrally-coordinated Fe^{2+} in Fe-doped MgO gives rise to an absorption feature near 380 that seems to be composed of a band at 378 nm due to octahedrally-coordinated Fe^{2+} and a more intense band at 381 nm due to non-octahedrally-coordinated Fe^{2+}. The most intense absorption feature associated with Fe^{2+} is a band centered near 253 nm that is attributed to octahedrally-coordinated Fe^{2+}–O charge transfer (Blazey, 1977).

The edge of the Fe–O charge transfer generally occurs at longer wavelengths for Fe^{3+} than Fe^{2+} (Soshea et al., 1958; Burns et al., 1976; Blazey, 1977; Smith, 1978; Keppler et al., 1994). Calculated energies of the highest wavelength Fe–O charge transfer transitions for Fe in octahedral coordination are 267 nm (37,500 cm^{-1}) for Fe^{2+} versus 395 nm (29,400 cm^{-1}) for Fe^{3+} (Tossell et al., 1974). The Fe^{3+}–O charge transfer is particularly intense and can be present in olivine spectra, even though Fe^{3+}/Fe^{2+} ratios of olivine are very low (Ullrich et al., 2002).

6. Results

The results of our UV spectral measurements are presented by major mineral groups. A number of these groups include multiple samples in the case of groups with solid solution series (e.g., olivine, pyroxene, plagioclase feldspar), and/or a range of grain sizes.

6.1. Meteoritic metal

A hand-ground <45 μm size powder of fusion crust- and alteration-free metal (Fe–Ni alloy) from the Odessa coarse octahedrite was included in this study. The spectrum was measured within 2 weeks of the grinding, thereby minimizing the formation of any iron oxide coating. Spectrally, the sample shows reflectance decreasing toward shorter wavelengths, with no significant superimposed metal–O absorption bands (Fig. 3a), as expected, and similar to reflectance spectra of comparable metals measured by other investigators (Dollfus et al., 1980; Wagner et al., 1987).

6.2. Hematite

Hematite (ideal formula Fe_2O_3) consists of octahedrally-coordinated sites occupied by Fe^{3+}, which should give rise to intense absorption bands near 230, 290, 345 and 395 nm (Loeffler

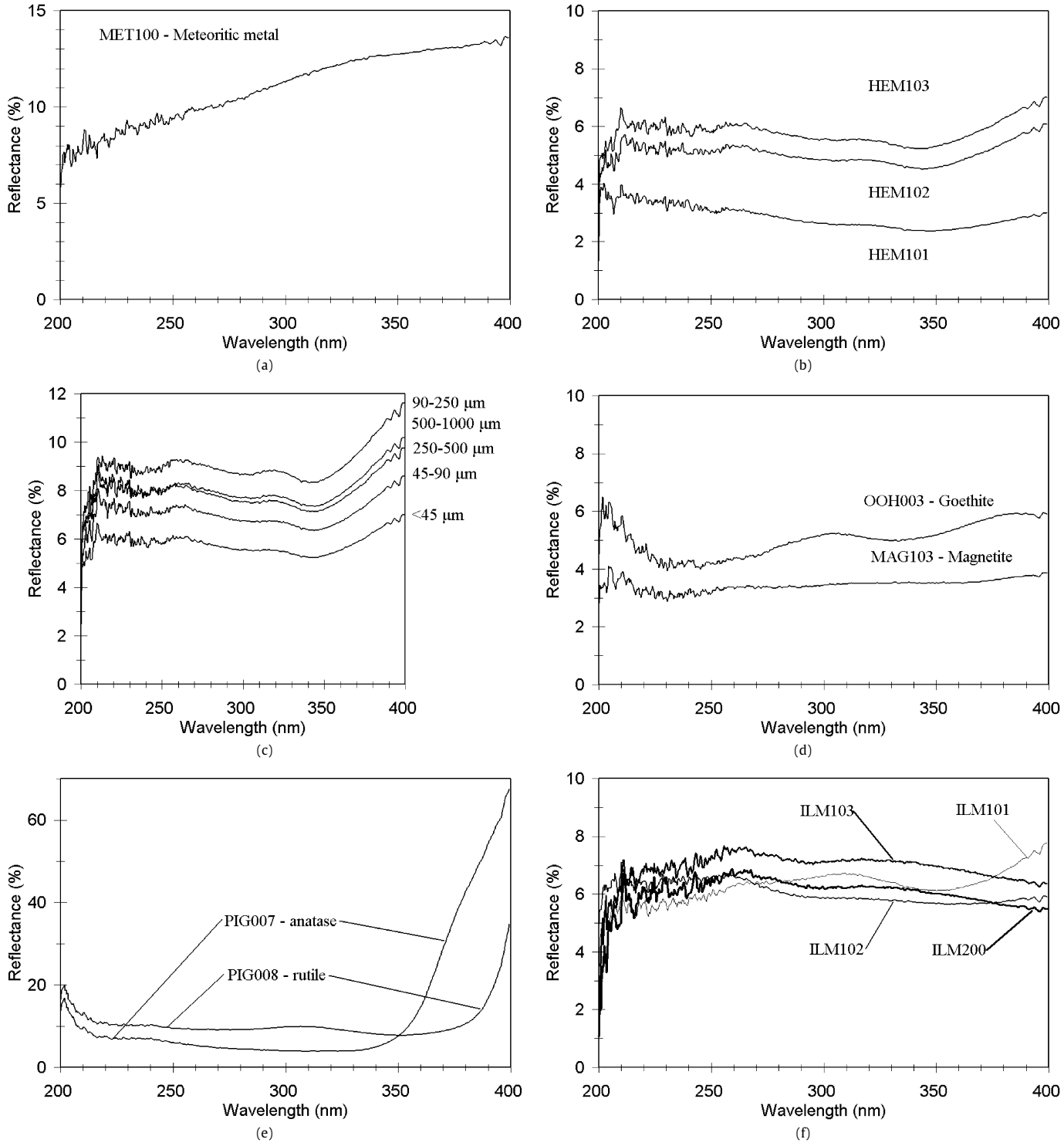

Fig. 3. Reflectance spectra (200–400 nm, unless otherwise indicated) of various samples: (a) meteoritic metal (MET100, <45 µm); (b) hematite (all <45 µm); (c) hematite (HEM103) for various grain sizes; (d) goethite (OOH003, <45 µm) and magnetite (MAG103, <45 µm); (e) TiO_2 polymorphs anatase (PIG007, <45 µm) and rutile (PIG008, <45 µm); (f) ilmenites (<45 µm); (g) same as (f) but for the 200–860 nm range (excluding ILM102); (h) ilmenite (ILM103) for various grain sizes; (i) same as (h) but for the 200–860 nm range; (j) palagonitic soils (<45 µm). Sample compositions are provided in Table 1.

et al., 1974; Tossell et al., 1974; Sherman and Waite, 1985). Reflectance spectra of three different hematites, as well as a series of different grain sizes of one hematite were measured (Figs. 3b–3c). All three hematites have low absolute reflectance and exhibit similar spectral features: reflectance maxima near 220, 265, and 320 nm, and generally poorly-defined and broad, shallow minima near 240, 280, and 345 nm. UV reflectance spectra of hematite measured by other investigators often show little spectral detail in this region, but most of the features seen in our spectra are also present in some other hematite spectra (Strens and Wood, 1979; Wagner et al., 1987). The absorption bands can all be assigned to Fe^{3+}–O charge transfers (Sherman and Waite, 1985). Increasing hematite grain size lead to a generally small increase in overall reflectance, but this increase is not systematic. In all cases, the reflectance maxima and minima do not change position appreciably, and remain equally well- (or poorly-) resolved for all grain sizes.

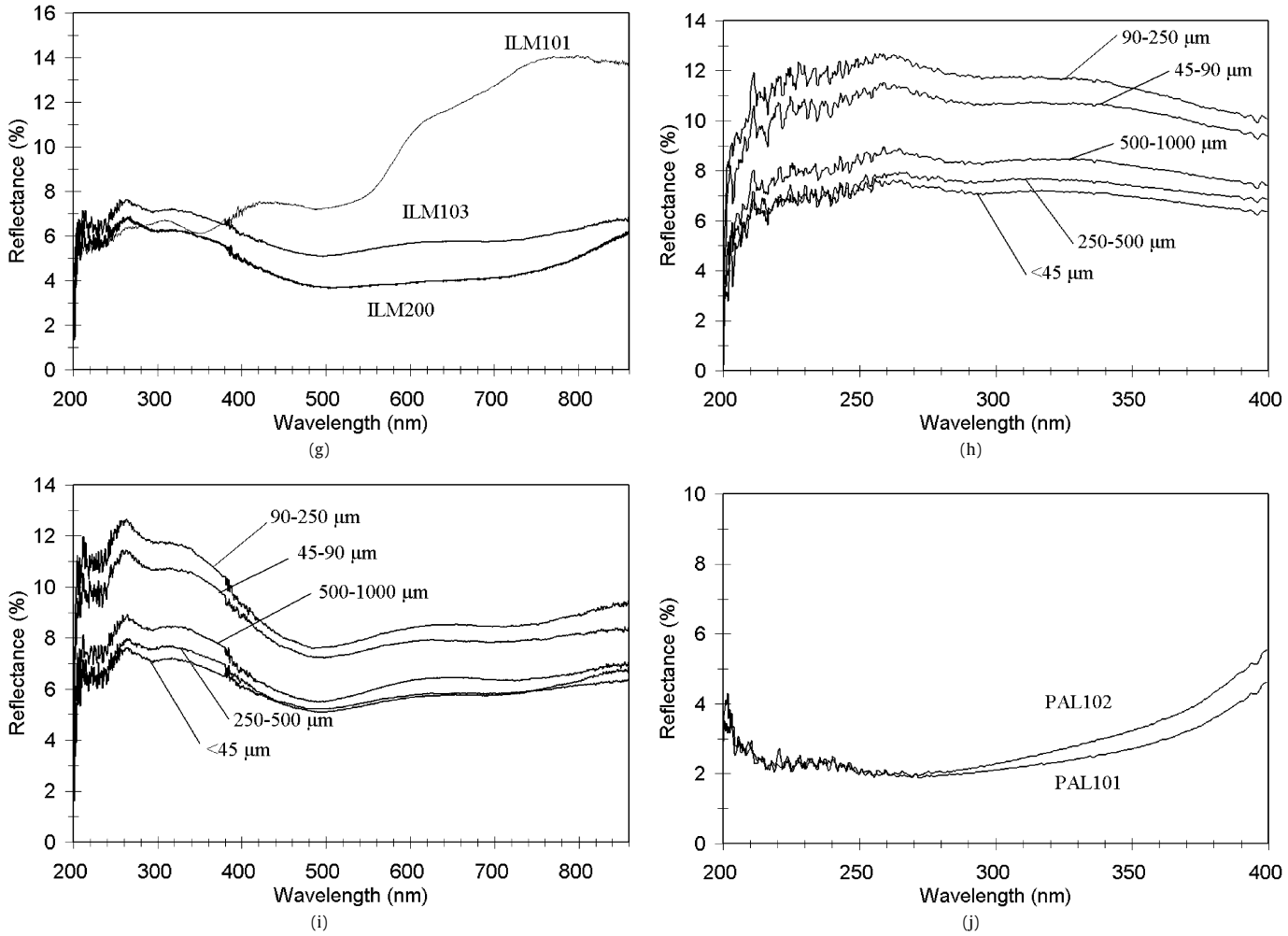

Fig. 3. (*continued*)

6.3. Goethite and magnetite

Goethite (*a*-FeOOH) consists of octahedrally-coordinated Fe^{3+}, with coordination provided by three O and three OH, thus we expect its UV spectrum to be dominated by Fe^{3+}–O absorption bands. Magnetite ($Fe^{2+}Fe_2^{3+}O_4$) consists of octatetrahedral sites occupied by both Fe^{3+} and Fe^{2+}, and tetrahedral sites occupied by Fe^{3+}. Both goethite and magnetite have been suggested as possible precursors to hematite on Mars (e.g., O'Connor, 1968; Gooding, 1978; Bell, 1992; Burns, 1993a; Christensen and Ruff, 2004). The UV spectrum of goethite (Fig. 3d) is characterized by absorption bands near 240 and 330 nm, attributable to an Fe^{3+}–O charge transfer and an Fe^{3+} spin-forbidden transition, respectively (Sherman and Waite, 1985). Our spectrum is similar to that of Strens and Wood (1979), but their major absorption band near 270 nm is only present as a shoulder on the more intense 240 nm absorption band in our spectrum. This likely arises from the differences in the way the published spectra were calculated from their laboratory measurements.

The magnetite UV spectrum (Fig. 3d) exhibits an absorption band near 230 nm, a broad, weak band between 270 and 290 nm, and an additional broad, weak feature near 350 nm. The overall decrease in reflectance toward shorter wavelengths and the absorption band near 230 nm are also seen in other magnetite spectra (Strens and Wood, 1979; Hapke et al., 1978; Wagner et al., 1987). The absorption coefficient of magnetite peaks near 230 nm (Pang et al., 1982). The absorption features can be attributed to octahedrally-coordinated Fe^{3+} and Fe^{2+} (Loeffler et al., 1974; Tossell et al., 1974).

6.4. Titanium dioxide

The two most common polymorphs of TiO_2, rutile and anatase, consist of octahedrally-coordinated Ti^{4+}, with different octahedral stacking. The structural differences should give rise to spectra with common absorption bands but possibly differing in position. Mariner 9 UV spectra of dust clouds have been interpreted as indicating the presence of a few percent of anatase, a TiO_2 polymorph (Pang and Ajello, 1977), based on decreasing absorption with increasing wavelength from 210 to 350 nm, a sharp absorption dropoff below 210 nm, and a "shoulder" between 240 and 250 nm. UV reflectance spectra may not be directly applicable to analysis of dust cloud spectra, but they can at least provide some guidance in the interpretation of such spectra. Our UV reflectance spectra (Fig. 3e) show differences in band positions that are likely attributable to structural differences. Both show a reflectance increase toward 210 nm, a shoulder (change in spectral slope) near 240 nm, and a sharp increase in reflectance longward of ~350 nm. The rutile spectrum shows weak absorption bands near 270 and 350 nm, with a local reflectance maximum near 305 nm, where the optical density is maximum (Bevan et al., 1958), and corresponds to a predicted reflectivity peak (Tossell et al., 1974). The anatase spectrum shows a broad region of absorption between ~260 and 340 nm region, with reflectance rising gradually to the inflection near 240 nm. To first order, anatase provides a reason-

able match to the spectral features in the Mars dust originally attributed to this mineral by Pang and Ajello (1977).

6.5. Ilmenite

Ilmenite ($FeTiO_3$) consists of octahedrally-coordinated sites occupied alternately by Fe^{2+} and Ti^{4+}. Hematite is a common accessory phase in terrestrial ilmenites, which consists of octahedrally-coordinated Fe^{3+}-occupied sites as discussed above. Pure ilmenite is expected to exhibit absorption bands near 260–270 and 300 nm (attributable to Fe^{2+}– and Ti^{4+}–O transitions). The presence of hematite will contribute additional absorption features near 217 nm and 340 nm.

None of the three natural ilmenite samples are pure, as all contain Fe^{3+} (Table 1); the synthetic sample is presumed to be pure stoichiometric $FeTiO_3$. Our ilmenite spectra (Figs. 3f–3g) and those of other investigators (Strens and Wood, 1979; Wagner et al., 1987) show variable spectral behavior. The ILM101 and 102 spectra indicate the presence of hematite, inferred from an absorption feature near 350 nm. The ILM103 and ILM200 spectra do not show this hematite feature: their spectra show reflectance increasing toward shorter wavelengths from 400 down to ~310 nm, generally flattening out between 310 and 250 nm, and then decreasing below ~250 nm. They both show weak reflectance maxima near 260 and 340 nm, consistent with the behavior of opaque minerals (Wagner et al., 1987; Hapke, 2001). Changing ilmenite grain size (ILM200) has no discernible effect on spectral shape, although overall reflectance does change by a few percent (Figs. 3h–3i). The ilmenite spectrum of Wagner et al. (1987) is of a natural terrestrial sample of unknown composition and its shape is broadly similar to that of the low-Fe^{3+} (ILM103) and synthetic ilmenite spectra, in particular the reflectance increase shortward of 400 nm. The reflectance spectrum of <25 μm size ilmenite powder (Hua et al., 1976) shows a slight increase in reflectance shortward of 400 nm, with local maxima near 250 and 330 nm and local minima near 230 and 350 nm. The synthetic ilmenite spectrum of Strens and Wood (1979) shows reflectance increasing shortward of 400 nm with absorption features near 300 (appearing as a shoulder) and 230 nm.

Overall these results indicate that ilmenite reflectance spectra are blue-sloped in the 250–400 nm range, likely due to the relative weakness of Fe^{2+}– and Ti^{4+}–O charge transfer bands near 270 and 360 nm compared to the major Fe^{2+}–Ti^{4+} charge transfer band near 500 nm (Strens and Wood, 1979). Reflectance would increase shortward of 500 nm as one moves away from this absorption band, and the Fe^{2+}– and Ti^{4+}–O charge transfer bands are comparatively weak enough to not result in an overall decrease in reflectance shortward of 400 nm. The decrease in reflectance shortward of ~250 nm is likely due to the combined effects of multiple metal–O charge transfers.

6.6. Palagonitic soil

Palagonitic soil is a largely amorphous material that is a spectral analogue for Mars dust (Morris et al., 2001). It is generally derived from devitrification of basaltic glass and is often colored orange-red by the presence of nanophase ferric oxides/oxyhydroxides, such as hematite and goethite, and possibly other phases (e.g., Morris et al., 1989, 1993, 2001), and hence its UV spectrum should be dominated by these phases. Both palagonitic soil samples used in this study exhibit similar UV spectra (Fig. 3j): a weak maximum near 240 nm and minima near 220 and 270 nm, with reflectance increasing toward longer wavelengths. These spectra differ from those of our hematite and goethite (perhaps not surprisingly, since the presumed coloring agent of palagonitic soil occurs in nanometer-sized grains instead of the tens of microns-scale grains of our hematite and goethite samples), but have some similarities to limonite: a weak maximum near 230 nm and an absorption band near 260 nm (Pang et al., 1982). Unfortunately, the weak spectral features are not particularly diagnostic of palagonitic soil and can plausibly be ascribed to plagioclase, which is the only crystalline material identified in these samples by X-ray diffraction (Banin et al., 1997; Morris et al., 2001).

6.7. Olivine

The dominant spectrally active metal in olivine [ideal formula: $(Mg,Fe)_2SiO_4$] is Fe^{2+}, with lesser amounts of Mn and Ni (Lumpkin and Ribbe, 1983). Mg and Fe occupy two roughly equivalent octahedrally-coordinated sites, M1 and M2, with an occasional slight enrichment of Fe^{2+} in the M2 site (Burns, 1970). Both Mn and Ni preferentially partition into the M2 site (Burns, 1970; Lumpkin and Ribbe, 1983). Fe^{3+} abundances in natural olivines are very low and any Fe^{3+} that is present would likely occupy the M1 site (Deer et al., 1997). Consequently, olivine UV spectra should be dominated by an Fe^{2+}–O charge transfer absorption band near 270 nm.

Smith and Langer (1982) measured single crystal transmission spectra of olivine and found an absorption feature near 295 nm that they attributed to Fe–O charge transfers. The edge of this absorption was found to move toward longer wavelengths with increasing Fe content. Cohen et al. (1978) and Wagner et al. (1979) show reflectance decreasing from 248 (2.8%) to 200 nm (2.5%) for powdered olivine, with a local minimum near 210 nm. By contrast, a powdered fayalite (the iron-rich olivine endmember) spectrum showed reflectance increasing from 248 to 200 nm (from 1.3 to 1.7%), and an inflection point near 220 nm. Wagner et al. (1987) found reflectance decreasing toward shorter wavelengths for <74 μm olivine powder and a local minimum near 215 nm. The reflectance spectrum of an olivine powder (<25 μm) measured by Dollfus et al. (1980) showed a decrease in reflectance to ~290 nm and generally flat reflectance at shorter wavelengths, while the reflectance spectrum of <25 μm olivine-bearing peridotite shows a decrease in reflectance toward shorter wavelengths and a local reflectance minimum near 260 nm (Dollfus et al., 1980).

The reflectance spectra of our olivine series for <45 μm size powders are shown in Fig. 4a. There is a general decrease in overall reflectance with increasing Fe^{2+} content. The lower Fe^{2+}-content olivines exhibit two reflectance minima near 217 and 250 nm, similar to the bands found by Cohen et al. (1978), Wagner et al. (1979), and Dollfus et al. (1980). Increasing Fe^{2+} content (from $Fa_{3.1}$ to $Fa_{99.9}$) results in a number of systematic spectral changes: the local reflectance maximum between the two absorption bands becomes less prominent; the band near 217 nm moves toward ~225 nm; the 250 nm band moves from 251 to 291 nm; and the overall spectral slope becomes less red-sloped, similar to the observations of Cohen et al. (1978) and Wagner et al. (1979). The increase in reflectance below ~250 nm for the $Fa_{99.9}$ olivine was also found by Wagner et al. (1979). The absorption feature near 217 nm is likely attributable to small amounts of Fe^{3+} that may be naturally present in the olivine or as a result of alteration, or possibly present in minor accessory phases.

As grain size increases for a single olivine, there is a gradual decrease in overall reflectance, and a loss of spectral contrast (Fig. 4b). The absorption band located near 250 nm exhibits a gradual shift toward longer wavelengths, and becomes much broader. The local maximum between the 215 and 250 nm peaks also becomes less prominent, resulting in a broad region of low overall reflectance. Below 250 nm, the spectrum becomes increasingly blue-sloped as grain size increases, similar to the results for polished surfaces and solid samples (Wagner et al., 1979).

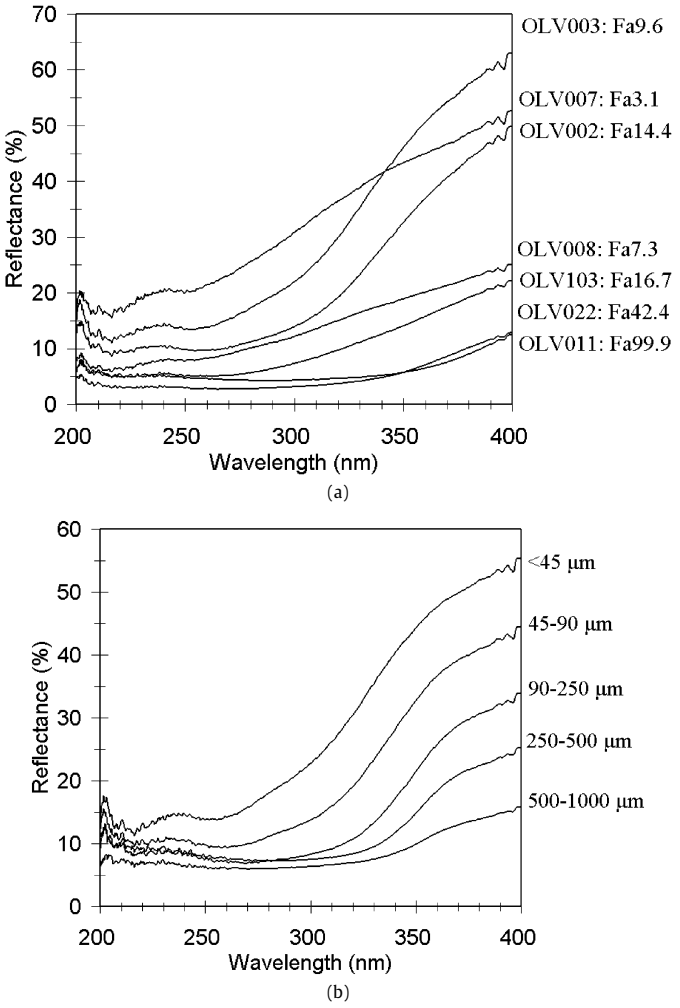

Fig. 4. Reflectance spectra (200–400 nm) of olivines: (a) as a function of composition (all <45 μm); and (b) OLV003 as a function of grain size. Sample compositions are provided in Table 1.

6.8. Pyroxene

Pyroxenes [ideal formula: $(Mg,Fe^{2+},Ca)SiO_3$], and in particular high-calcium pyroxenes (HCPs), can incorporate many transition series elements in two non-equivalent octahedrally-coordinated sites, M1 and M2. The most important cation is Fe^{2+}, although many terrestrial HCPs can also incorporate substantial amounts of Fe^{3+} into their structure. In low-calcium pyroxene (LCPs), Fe^{2+} largely occupies the M2 site. In HCPs, Ca is more strongly partitioned into the M2 site, with Fe^{2+} making up any deficiencies, and the remainder partitioned into the M1 site; Fe^{3+} preferentially occupies the M1 site (Cloutis, 2002, and references therein).

The spectra of both LCP and HCP <74 μm powders show reflectance decreasing toward shorter wavelengths but with different rates of decrease (Wagner et al., 1987). Some LCPs exhibit a weak absorption band, appearing as an inflection, near 250 nm, while HCPs have a weak band near 270–280 nm. Reflectance spectra of <25 μm powders of two pyroxene-rich achondrites (Kapoeta howardite and Tataouine diogenite) both exhibit reflectance decreasing toward shorter wavelengths and a few weak superimposed absorption features (appearing as inflections) near 250 and 300 nm, and a more well-defined absorption band near 220 nm (Hua et al., 1976). Reflectance spectra of two eucrites (HCP-rich, <200 μm grain sizes) show reflectance decreasing below 400 nm, with Chernovy Kut exhibiting minimum reflectance near 300 nm while Stannern showed reflectance continuing to decrease to at least 260 nm (Shkuratov et al., 1985).

Our LCP reflectance spectra (Fig. 5a) are characterized by rapidly decreasing reflectance toward shorter wavelengths and two broad absorption bands near 220 and 250 nm for the <45 μm fractions, similar to the results of Hua et al. (1976). These bands are likely attributable to Fe^{3+}– and Fe^{2+}–O charge transfers, respectively. With increasing Fe^{2+} content, overall reflectance decreases and the absorption bands become broader and less well-defined, consistent with increasing Fe^{2+} content causing a progressive deepening of the absorption band. The absorption bands near 220 nm appears to shift from ~216 to 225 nm with increasing Fe^{2+} content, although the band is not well defined in the higher Fe^{2+}-content sample spectra. The 250 nm absorption band does not exhibit a systematic shift in position, occurring between ~245 and ~255 nm in all cases.

With increasing grain size (PYX032; Fs 41.5), resolution of the absorption bands becomes more difficult and overall reflectance decreases (Fig. 5b). We found that the largest grain size (500–1000 μm) spectrum has higher-than-expected reflectance, perhaps due to enhanced specular reflection. When normalized, this spectrum shows the largest band depth, as expected. There are no apparent systematic shifts in the absorption band positions with changes in grain size, although the two major absorption features are not well resolved.

HCP spectra are more difficult to interpret. This is due to the presence of appreciable amounts of both Fe^{3+} and Fe^{2+} in most terrestrial samples as well as the availability of two distinct crystallographic sites that can be occupied by Fe^{2+} and other cations. Fe^{2+} site occupancies determine whether the HCP is of spectral type A or B (Adams, 1974). Fourteen HCPs were included in this study, seven of each spectral type. Our search for spectral–compositional correlations included separating and aggregating spectral type A and B and examining spectral properties as a function of both Fe^{2+} and Fe^{3+} content.

This analysis yielded a number of general observations. Both spectral type A and B HCPs exhibited similar spectral shapes (reflectance decreasing from 400 to ~250 nm and flat or slightly blue below this value) and absorption bands (two bands near 220 and 270 nm). For spectral type A (Fig. 5c), overall reflectance in the 200–400 nm range was better correlated with Fe^{3+} content than Fe^{2+} content. All the spectra showed two absorption bands near 220 nm and 270 nm; the minimum of the 220 nm band varied between 220 and 225 nm with the higher Fe^{2+} and Fe^{3+} sample spectra generally exhibiting the band closer to 225 nm. The 270 nm band minimum varied between 270 and 275 nm with the higher Fe^{2+} and Fe^{3+} sample spectra generally exhibiting the band closer to 275 nm.

For spectral type B HCPs (Fig. 5d), Fe^{2+}, rather than Fe^{3+}, content appears to be more strongly correlated with overall reflectance, although overall reflectance variations are small for higher Fe-content samples. The spectra exhibit two absorption bands near 220 and 270 nm. The 220 nm region band has a minimum generally between 220 and 225 nm, similar to the type A HCPs, although the noise in the data and the weakness of the feature precludes identification of more precise minima in many cases. The 270 nm absorption feature minimum occurs between ~250 and 270 nm and is more correlated with Fe^{3+} content than Fe^{2+} content. The band occurs at generally longer wavelengths for the more Fe^{3+}-rich samples, although the range of Fe^{3+} contents is small for these samples (0.00–2.03 wt% Fe_2O_3). It should be noted that Fe^{3+} could occupy both tetrahedral and octahedral sites in HCPs.

When the HCP spectra are aggregated, the following correlations emerge: the Fe^{3+}-free samples are substantially brighter than those containing detectable amounts of Fe^{3+}. This is consistent

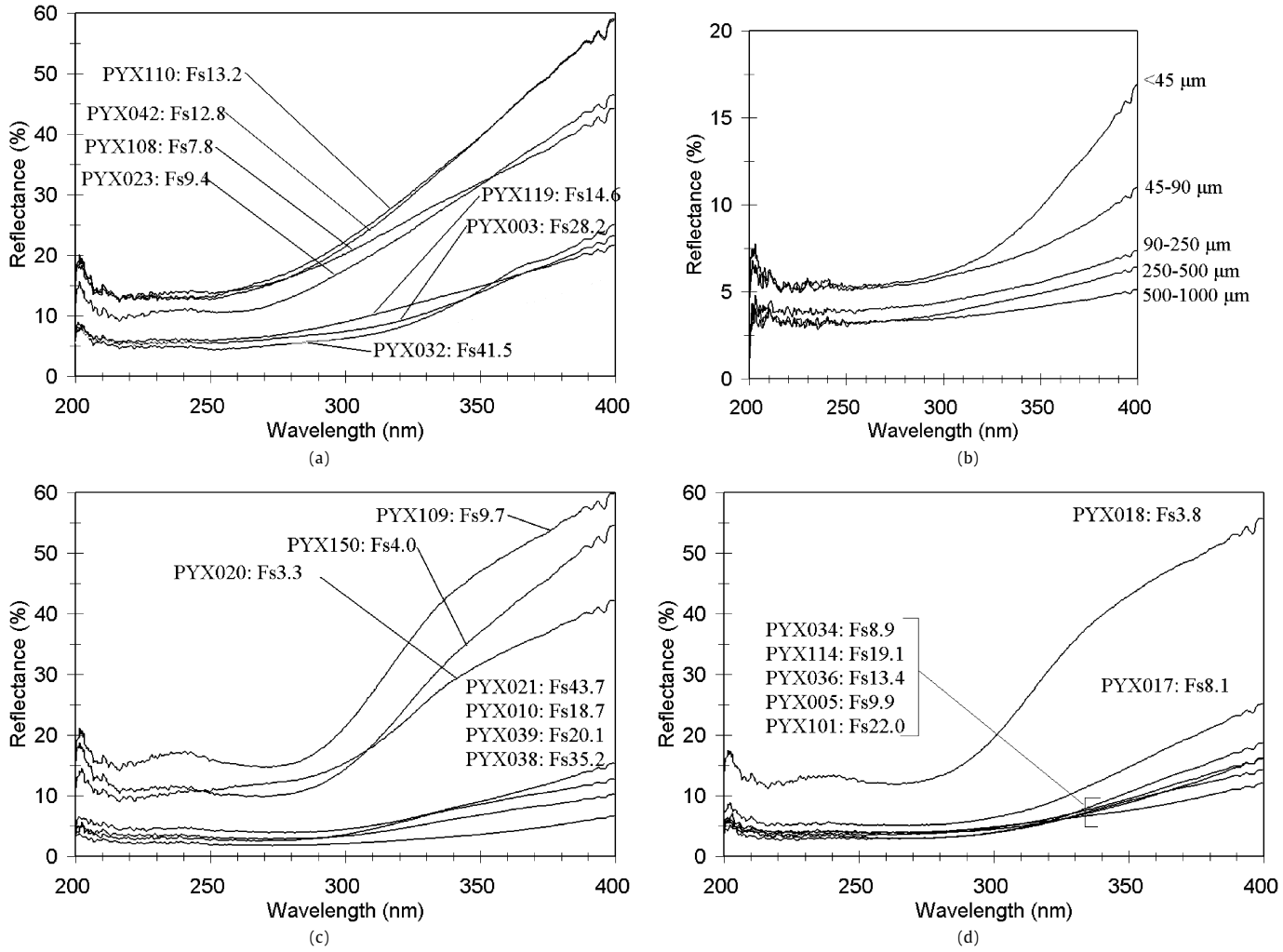

Fig. 5. Reflectance spectra (200–400 nm) of pyroxenes: (a) low-calcium pyroxenes (<45 µm); (b) low-calcium pyroxene PYX032 for various grain sizes; (c) spectral type A high-calcium pyroxenes (<45 µm); (d) spectral type B high-calcium pyroxenes (<45 µm). Sample compositions are provided in Table 1. Ferrosilite contents (mol% Fs) are indicated for each sample in (a), (c), and (d).

with the wide-ranging spectral-darkening effect of Fe^{3+}, whose broad absorption band extends into the visible region (Blazey, 1977; Smith, 1978; Keppler et al., 1994). The wavelength positions of both the 220 and 270 nm absorption bands generally increase with increasing Fe^{3+} content, although a well-defined trend could not reliably be constructed due to noise in the 220 nm region and the broad and shallow nature of the 270 nm absorption feature in many of the spectra.

6.9. Plagioclase feldspar

The major spectrally active metal in plagioclase feldspar [ideal formula: $(Na,Ca)(Si,Al)_4O_8$] is Fe, which may occur as Fe^{3+} substituting for Al in the tetrahedral site, or as Fe^{2+} in the larger 7-coordinated site in the case of lunar rocks and meteorites (Burns, 1993b; Deer et al., 2001). Thus, in most terrestrial plagioclase feldspar spectra we can expect absorption bands attributable to both Fe^{3+}–O and Fe^{2+}–O transitions.

The reflectance spectra of terrestrial plagioclase feldspars measured by Carver et al. (1975) exhibited diverse spectral behavior. One sample (their #4, anorthosite, 90% plagioclase) showed reflectance gradually decreasing from 11% at 400 nm to 6% at 200 nm, with inflections near 240 and 300 nm. A second sample (their #17; brecciated anorthosite) showed reflectance decreasing from 6% at 400 nm to 1.8% at 200 nm with the spectrum progressively flattening out toward shorter wavelengths. Another sample (their #12; anorthosite; fine-grained, almost pure anorthite) exhibited reflectance decreasing from 7% at 400 nm to ~5% at 200 nm, and minimum reflectance near 210 nm. A fourth sample (their #25, albite) showed reflectance decreasing from ~6% at 400 nm to ~4% at 200 nm, with a reflectance minimum near 250 nm. A chip of Apollo 16 anorthosite shows reflectance decreasing from 248 to 200 nm (from 2.7 to 1.6%) (Hapke et al., 1978). The spectra of two plagioclase feldspar powders measured by Wagner et al. (1987) show reflectance decreasing toward shorter wavelengths over the 200 to 400 nm range. Inflections and local minima are present near 230 and 390 nm in at least one of the spectra. The reflectance spectrum of <25 µm anorthosite powder shows reflectance decreasing toward shorter wavelengths with a minimum near 230 nm (Dollfus et al., 1980). Thus, we expect plagioclase feldspar powders to be red-sloped over the 200–400 nm interval.

We examined plagioclase feldspar spectra as a function of both grain size and composition. There is a general correlation between anorthite and iron content (Adams and Goullaud, 1978). Given that absorption in the UV is attributable to Fe–O charge transfers, we examined spectral changes as a function of Fe content. As Fe content increases, overall reflectance decreases in the UV, and more well-defined absorption bands appear (Figs. 6a–6b). The reflectance decrease is consistent with transmission spectra (Bell and Mao, 1973). The absorption bands are located near 225 and 250 nm,

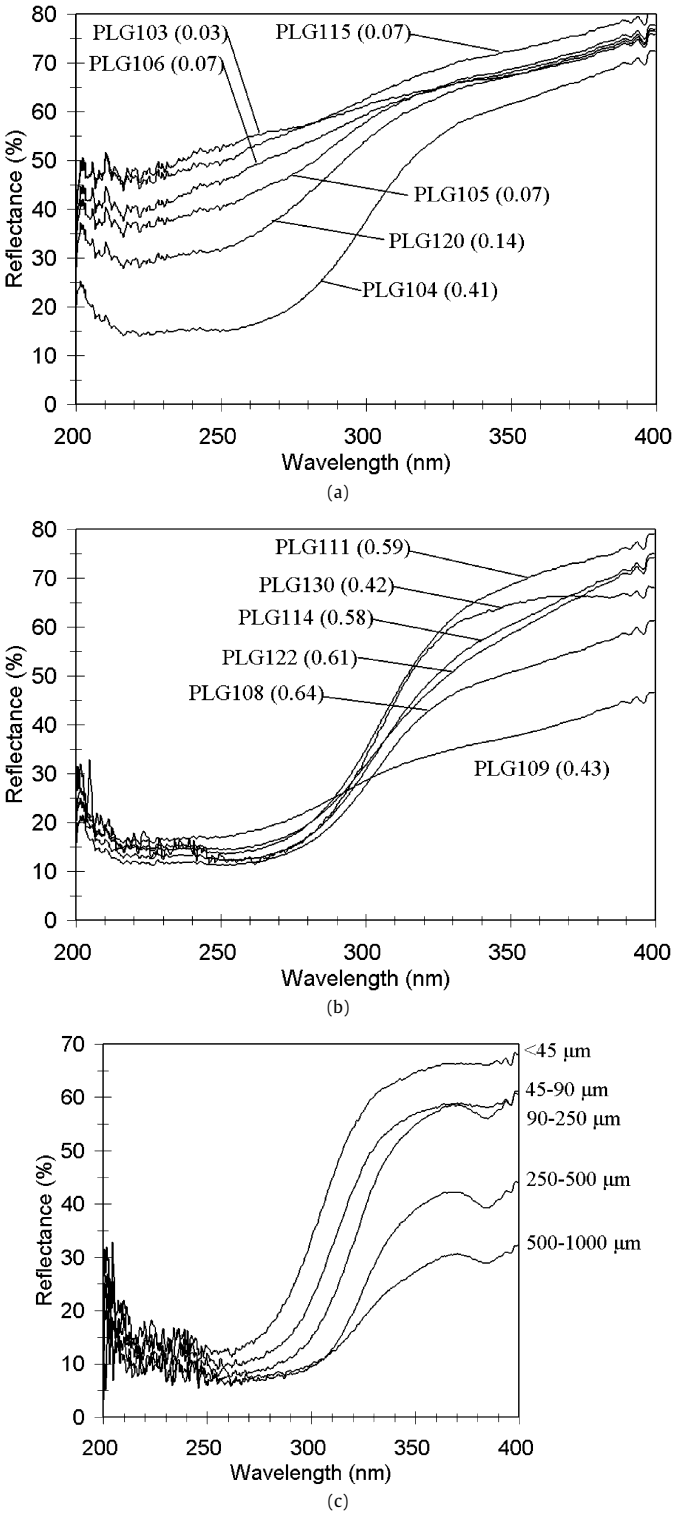

Fig. 6. Reflectance spectra (200–400 nm) of plagioclase feldspars: (a) for the lower Fe-content members (<45 μm); (b) for the higher Fe-content members (<45 μm); (c) PLG130 reflectance spectra as a function of grain size. Fe content (as wt% Fe_2O_3) is indicated for each sample. Sample compositions are provided in Table 1.

although the local reflectance maximum between these two features is not prominent in the most Fe-rich samples. The presence of these two features is consistent with contributions from both Fe^{3+} (~225 nm) and Fe^{2+} (~250 nm).

These results are similar to the features found by other investigators (Carver et al., 1975; Dollfus et al., 1980; Wagner et al., 1987).

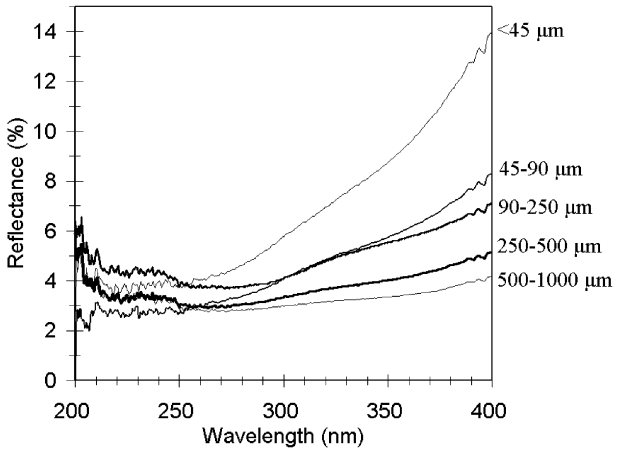

Fig. 7. Reflectance spectra (200–400 nm) of basalt SA-51 for different grain sizes. Sample composition is provided in Table 1.

The weak and narrow absorption features seen below ~240 nm in our spectra are attributable to artifacts from the UV mirror and low signal-to-noise. Both major bands seem to shift to slightly longer wavelengths with increasing Fe content, although the bands are only well resolved in the more Fe-rich sample spectra. The bands occur near 225 and 253 nm in these samples versus ~215 and 250 nm in the Fe-poor sample spectra. The absorption bands are too broad and the shifts too small to derive a reliable correlation with Fe content.

With increasing grain size (Fig. 6c) plagioclase feldspar shows a decrease in overall reflectance, accompanied by a gradual movement of the "absorption edge" (where reflectance begins to increase) toward longer wavelengths. The larger grain size spectra also show the increasing prominence of an absorption feature near 380 nm that is likely attributable to octahedrally-coordinated Fe^{2+} (Blazey, 1977). Band minima are located near 225 (presumably attributable to Fe^{3+}) and 253 (Fe^{2+}) nm and do not show changes in position with grain size variations.

6.10. Basalts and gabbros

These rock types are dominated by mafic silicates and plagioclase feldspar, and are expected to exhibit UV absorption features attributable to both Fe^{2+} and Fe^{3+} located in the various constituent minerals: i.e., absorption bands near 220 and 270 nm. Basalts and gabbro slabs exhibit calculated albedos between 1 and 8% in the 200–400 nm region (Carver et al., 1975) with reflectance decreasing toward shorter wavelengths, and exhibiting a local reflectance minimum between 190 and 230 nm. The spectra of the two basalts and one gabbro included in their study show differences in the positions of absorption bands and inflection points. For pulverized lunar rocks, which include gabbro and basalt, all exhibit reflectance decreasing toward shorter wavelengths over the 200–400 nm interval (Hapke et al., 1978), and some exhibit local minima near 220 nm, similar to the spectral behavior of lunar fines. Once again, there is no consistency between the various lunar rocks. Hapke et al. (1978) attribute specific absorption features to various charge transfers: 250 nm to Fe^{2+}–O^{2+}, and 340 nm to Fe^{2+}–Ti^{4+}. The reflectance spectra of a gabbro slab and various sizes of powder measured by Greenman et al. (1967) show reflectance generally decreasing from 300 to 250 to 200 nm (the three wavelengths for which reflectance values are tabulated), although the magnitude of the decrease differed depending on which spectrometer was used for the measurements.

Basalts are a useful material to examine the ways that reflectance spectra of rocks may differ from those of the constituent minerals. Reflectance spectra of a series of grain sizes of a

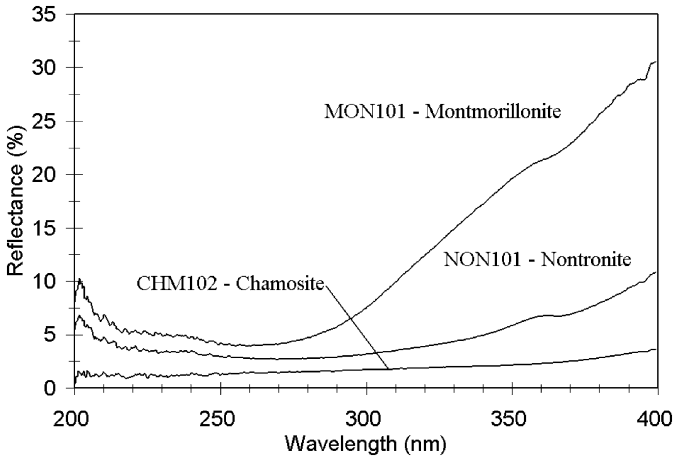

Fig. 8. Reflectance spectra (200–400 nm) of phyllosilicates (<45 μm). Sample compositions are provided in Table 1.

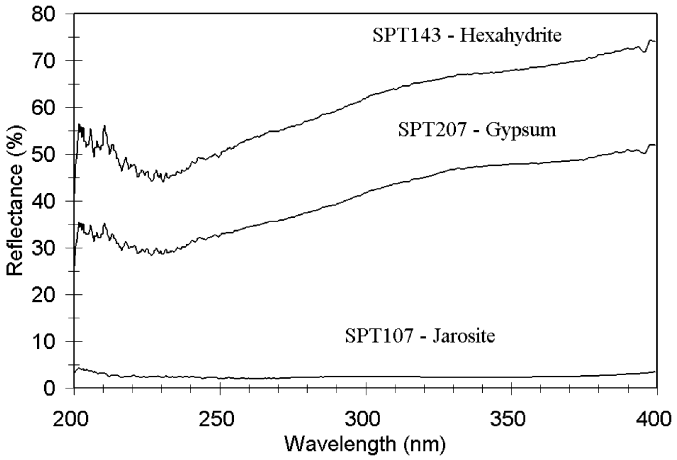

Fig. 9. Reflectance spectra (200–400 nm) of sulfate minerals (<45 μm). Sample compositions are provided in Table 1.

Columbia River basalt (Atkinson, 1990), are shown in Fig. 7. As was the case for the mafic minerals, overall reflectance generally decreases and overall spectral slope becomes shallower with increasing grain size. There are suggestions of an inflection near 320 nm, and an absorption band in the 250–270 nm region whose position increases with increasing grain size. These features are also seen in basalt spectra from other investigators (Carver et al., 1975; Hua et al., 1976). The basalt sample is volumetrically dominated by plagioclase feldspar (An ~58) with lesser amounts of augite, and subordinate olivine and various oxides (Atkinson, 1990). The inflection and absorption bands in the basalt spectra cannot be uniquely assigned to any one constituent mineral, as they are common to many of the minerals included in this study.

6.11. Phyllosilicates

As with most other minerals, the UV spectral properties of phyllosilicates will be largely dictated by the nature of any transition series elements that are present. Metals in phyllosilicates are normally present in octahedrally-coordinated sites. Ground-based telescopic and Phobos-2 ISM spectra of Mars were used to identify possible metal–OH absorptions occurring in phyllosilicates or other hydrated minerals on Mars (e.g., Clark et al., 1990; Murchie et al., 1993; Bell and Crisp, 1993; Bell et al., 1994). More recently, the Mars Express OMEGA spectrometer has detected evidence for specific phyllosilicates on Mars, including chamosite (Mg, Fe^{2+}, Fe^{3+} bearing), montmorillonite (Na, Ca, Al, Mg bearing), and nontronite (Fe^{3+} bearing) (e.g., Poulet et al., 2005).

The two Fe-bearing phyllosilicates [chamosite (ideal formula: $(Fe^{2+},Mg,Fe^{3+})_5Al(Si_3Al)O_{10}(OH,O)_8$) and nontronite (ideal formula: $Na_{0.3}Fe_2^{3+}(Si,Al)_4O_{10}(OH)_2{\cdot}n(H_2O)$)] exhibit lower overall reflectance than the Fe-poor montmorillonite, as expected (Fig. 8). The montmorillonite [ideal formula: $(Na,Ca)_{0.3}(Al,Mg)_2Si_4O_{10}(OH)_2{\cdot}n(H_2O)$] and nontronite spectra exhibit absorption bands attributable to Fe^{3+} (~220 nm) and Fe^{2+} (~260, ~370 nm) (Sherman and Vergo, 1988). The chamosite spectrum does not exhibit any well-defined reflectance minima, likely due to the presence of appreciable Fe^{3+} and Fe^{2+}, which lowers overall reflectance. An overall reflectance decrease in montmorillonite spectra has also been seen by Dollfus et al. (1980).

6.12. Sulfates

The UV spectral properties of sulfates will be largely determined by their spectrally active metal contents. Fe is the most abundant metal in common terrestrial sulfates, occurring most often as Fe^{3+} (Hawthorne et al., 2000). Martian sulfates have been tentatively identified from ground-based and spacecraft observations (e.g., Burns, 1987; Blaney and McCord, 1989; Pollack et al., 1990; Morris et al., 2000; Bandfield, 2002), More recently, analysis of Mars Express OMEGA spectrometer data has indicated the presence of a specific polyhydrated sulphate, gypsum, and kieserite deposits (Gendrin et al., 2005; Langevin et al., 2005), while jarosite has been detected by Mossbauer spectroscopy on the Mars Exploration Rover Opportunity (e.g., Klingelhöfer et al., 2004).

We have measured the UV spectral reflectance properties of jarosite [ideal formula: $(K,Na)Fe_3^{3+}(SO_4)_2(OH)_3$], hexahydrite [a polyhydrated sulphate; ideal formula: $MgSO_4{\cdot}6(H_2O)$], and gypsum [ideal formula: $CaSO_4{\cdot}2(H_2O)$] (Fig. 9) to assess whether UV observations are also capable of detecting and discriminating these minerals. The gypsum and anhydrite spectra both exhibit a reflectance minimum at 225 nm and a weak inflection near 330 nm, and are largely indistinguishable from each other, likely due to the low abundance of spectrally active transition series elements in these samples. These features are likely attributable to Fe^{3+}–O charge transfers, since this is the most intense metal–O absorption and even trace amounts of Fe^{3+} could give rise to Fe^{3+}–O charger transfers. The jarosite spectrum exhibits minima near 225, 262 and 340 nm, and is unlike the other minerals included in this study. These features are likely all attributable to Fe^{3+}–O charge transfers (Sherman and Waite, 1985).

7. Discussion of laboratory spectra

As demonstrated above, the UV reflectance spectra of common rock-forming minerals are dominated by metal–O charge transfer absorptions, with the most common metal being Fe. The intensity and wavelength position of UV absorption bands will be determined by the types and abundances of the metals, oxidation state, and their coordination environment. The strongest Fe^{3+}–O and Fe^{2+}–O charge transfer bands occur near 217 and 250 nm, respectively, and the vast majority of the mineral spectra in this study exhibit both of these features. As the Fe^{3+}–O absorption is approximately two orders of magnitude more intense than a comparable Fe^{2+}–O charge transfer band, this feature appears even in minerals with low Fe^{3+} abundances, such as LCP and olivine. The wavelength positions of the resolvable absorption bands in the measured mineral spectra are shown in Fig. 10. It is immediately apparent that the various Fe-bearing silicates are highly overlapped, and all cluster in the region defined by the major Fe^{3+} (~220 nm) and Fe^{2+} (~250 nm) absorption bands. This suggests that Fe-bearing silicates are not easily discriminated solely on the basis of UV band minima positions.

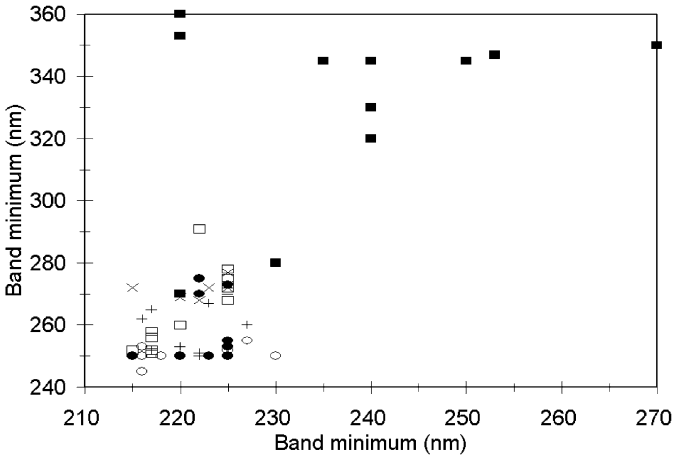

Fig. 10. Wavelength positions of the band minima for the samples used in this study (see Table 3). The lowest and highest wavelength bands have been plotted for the hematites; the weak and broad band near 290 nm has been omitted. Symbols: filled squares: oxides, hydroxides; open squares: olivines; closed circles: plagioclase feldspars; open circles: low-calcium pyroxenes; crosses: spectral type B high-calcium pyroxenes; X: spectral type A high-calcium pyroxenes; dashes: basalts. Both compositional and grain size variations are included for each mineral group where available.

Further complicating mineral identification using Fe–O charge transfer band positions is grain size. Increasing grain size has a number of effects on reflectance spectra in the UV. The intensity of the Fe^{3+}–O charge transfer, in particular, indicates that even small amounts of Fe^{3+} can result in UV absorption bands that appear to be saturated. Saturated absorption bands can be recognized by low overall reflectance (generally in the range of a few %) and asymmetric-appearing absorption features. Many of the minerals included in this study are suggestive of saturated absorption bands in the 210–250 nm region. With increasing abundance of Fe, either due to larger grains (resulting in more volume versus surface scatter) or greater Fe abundance, Fe absorption bands become increasingly broad, and this manifests itself as a gradual shift in the edge of the rise in reflectance toward longer wavelengths, often accompanied by a shift in apparent band minimum toward longer wavelengths. The shift in band position likely arises from a combination of the UV band becoming broader as saturation increases or as it becomes more intensely coupled with adjacent higher wavelength bands that become progressively deeper, thereby "dragging" the UV band minimum toward longer wavelengths. This can be seen by comparing the montmorillonite and nontronite spectra (Fig. 8). The two minerals are essentially isomorphous, but the nontronite is more Fe-rich than the montmorillonite. The higher Fe content in the nontronite results in the main band minimum occurring at longer wavelengths (~270 nm in nontronite vs ~260 nm in montmorillonite).

The results for the different mineral species allow us to assess how grain size and compositional changes affect UV reflectance spectra. The plagioclase feldspar spectra show higher overall UV reflectance compared to the olivines and pyroxenes, suggesting that they are not saturated in the UV. They do not show any reliable systematic correlations between wavelength position and either Fe content or grain size, suggesting that Fe–O band positions are insensitive to either of these factors for unsaturated spectra. This is consistent with the nature of metal–O charge transfer bands, whose positions depend only on the covalency of the metal–O interaction (Sherman, 1983). By contrast, the olivine spectra have much lower overall UV reflectance and do show a shift of the main 250 nm region absorption band to longer wavelengths with both increasing Fe^{2+} content and increasing grain size.

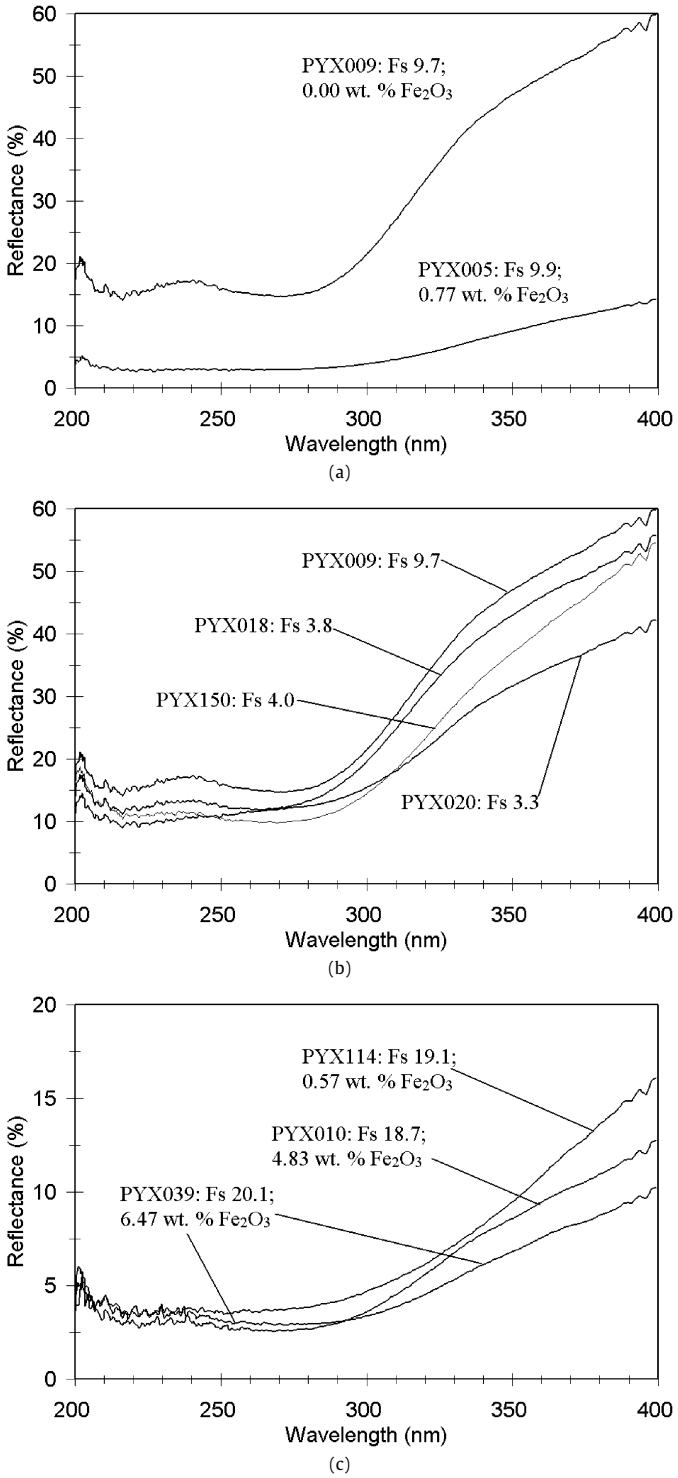

Fig. 11. Reflectance spectra of three different sets of high-calcium pyroxenes: (a) two samples with similar Fe^{2+} but different Fe^{3+} contents: PYX005 and 009; (b) four samples with no apparent Fe^{3+} from wet chemical analyses (PYX009, 018, 020, and 150); and (c) three samples with similar Fe^{2+} but different Fe^{3+} contents (PYX010, 039, 114).

The sensitivity of the UV spectral region to low abundances of transition series elements, particularly Fe^{3+}, can be gleaned from the spectral data for the lowest Fe-content samples, as well as comparisons of HCP spectra of similar compositions. The spectra of PYX005 (Fs 9.9, 0.77 wt% Fe_2O_3) and PYX009 (Fs 9.7, 0.00 wt% Fe_2O_3) are shown in Fig. 11a. Even though the PYX009 spectrum shows only a very small (~1% band depth) Fe^{2+}–Fe^{3+} charge

transfer absorption near 0.75 μm, it does exhibit an absorption feature near 215 nm, attributable to Fe^{3+}–O charge transfers. PYX005, containing 0.77 wt% Fe_2O_3, has a more intense Fe^{3+}–O charge transfer, as evidenced by the low overall reflectance across the entire 200–400 nm range and the lack of a well-defined Fe^{3+}–O band near 215 nm.

Examining the reflectance spectra of the HCPs that appear to be Fe^{3+}-free by wet chemical analysis (PYX009, 018, 020, and 150), we find that all four spectra exhibit an Fe^{3+}–O charge transfer absorption near 215 nm, in spite of very low Fe^{3+} contents (Fig. 11b). Comparing the reflectance spectra of three HCPs with similar Fe^{2+} contents—PYX114 (Fs 19.1, 0.57 wt% Fe_2O_3), PYX010 (Fs 18.7, 4.83 wt% Fe_2O_3), and PYX039 (Fs 20.1, 8.70 wt% Fe_2O_3)—we see that increasing Fe^{3+} content results in a decrease in overall reflectance and the wavelength position of the reflectance minimum in the 270 nm region to move to longer wavelengths (Fig. 11c). This indicates that the UV spectral region can serve as a very sensitive indicator of even trace amounts of Fe^{3+}; whether this sensitivity extends to other transition series elements has not been assessed.

The spectrum-altering effects of Fe^{3+} can also be gauged from comparison of HCP spectra. PYX005 and 009 differ primarily in Fe^{3+} content (Fig. 11a; Table 1). The higher Fe^{3+} content of PYX005 translates into lower overall reflectance across the entire 200–400 nm, and extends well into the near-infrared region (Blazey, 1977). The spectrum-altering effect of Fe^{3+} appears to be most pronounced at low Fe^{3+} abundances. The spectra of PYX114, 010, and 039, which contain progressively increasing amounts of Fe^{3+} are more similar in the 200–400 nm region than PYX005 versus PYX009, suggesting that "saturation" of the Fe^{3+}–O charge transfer band occurs at low Fe^{3+} abundances, and that the spectral changes are more gradual beyond the few percent Fe^{3+} level.

The spectral domination of Fe^{3+} relative to Fe^{2+} and the insensitivity of the position of Fe–O charge transfers to small changes in coordination site symmetry (Sherman, 1983) indicate that most minerals that contain Fe^{3+} and Fe^{2+} will exhibit absorption bands near 220 and 260 nm. As a result, band minima do not provide a reliable means to separate different mineral species (Fig. 10). When combined with the shifts in band minima that can occur due to band saturation, arising either from increases in Fe content or changes in grain size, the use of UV band minima for mineral identification is further degraded. As an example, band minima in the 260 nm region of <45 μm size olivine moves to longer wavelengths with increasing Fe content as well as with increasing grain size (Table 3). UV band positions alone are insufficient to distinguish an increase in Fe^{2+} content from an increase in grain size in this case. The minerals with unsaturated absorption bands do not exhibit shifts in band positions with changes in Fe content for unsaturated absorption bands. Spectra with saturated bands (e.g., hematite) also do not exhibit consistent shifts in minima positions with variations in composition or grain size.

One factor that could potentially be used to separate out the effects of increasing grain size from band saturation is the intensification of weaker Fe–O absorption bands. As seen in the reflectance spectra of the plagioclase feldspar grain size series (Fig. 6c), the weak 370 nm Fe^{2+}–O charge transfer band becomes progressively deeper with increasing grain size. However, a rigorous analysis of the intensification of weak bands with grain size increases is beyond the scope of this paper.

In spite of these limitations, the fact remains that absorption bands attributable to different metals and coordination environments are sometimes unique. This is most evident in the rutile and anatase spectra, where Ti^{4+}–O charge transfer bands occur in different positions for these two spectra in spite of identical compositions and coordination environments, but differing only in the arrangement of the octahedrally-coordinated sites. Thus, it would be possible in some situations to identify specific metal-coordination environments. However, specific mineral identification is largely elusive using only the UV region, given the overlaps in absorption bands for different mineral groups, the intense na-

Table 3
Wavelength positions of band minima in the UV

Mineral	wt% FeO	wt% Fe_2O_3	Grain size (μm)	Band minima (nm)		
Hematites						
HEM101	0.19	97.40	<0.14	253	~290	347
HEM102	0.91	96.66	<45	250	~290	345
HEM103	1.33	96.35	<45	250	~290	345
HEM103	1.33	96.35	45–90	240	~290	345
HEM103	1.33	96.35	90–250	240	~290	345
HEM103	1.33	96.35	250–500	240	~290	345
HEM103	1.33	96.35	500–1000	235	~290	345
Goethite						
OOH003		89.29[a]	<45	240	330	
Magnetite						
MAG103	28.80	60.38	<45	230	280	350
TiO_2 polymorphs						
PIG007	0.00	0.00	<45	240	320	
PIG008	0.00	0.00	<45	270	350	
Ilmenites						
ILM101	1.38	33.05	<45	220	353	
ILM101	1.38	33.05	45–90	220	353	
ILM102	24.64	18.61	<45	220	360	
Palagonitic soil						
PAL101	2.77	12.58	<45	220	270	
PAL102		13.1[a]	<45	220	270	
Olivines						
OLV007	3.12[b]		<45	217	251	
OLV008	7.15	0.00	<45	215	252	
OLV003	9.25	0.59	<45	217	252	
OLV003	9.25	0.59	45–90	217	258	
OLV003	9.25	0.59	90–250	225	272	
OLV003	9.25	0.59	250–500	225	278	
OLV003	9.25	0.59	500–1000	225	275	
OLV002	13.92[b]		<45	217	256	
OLV103	15.88[b]		<45	220	260	
OLV022	36.37[b]		<45	225	268	
OLV011	66.48[b]		<45	222	291	
Low-calcium pyroxenes						
PYX108	5.29	1.13	<45	216	250	
PYX023	6.36	0.83	<45	216	253	
PYX042	8.93	0.84	<45	216	250	
PYX110	9.19	0.44	<45	216	245	
PYX119	9.92	0.72	<45	218	250	
PYX117	16.17	1.02	<45	225	252	
PYX003	17.30	1.43	<45	225	250	
PYX032	23.65	5.11	<45	225	250	
PYX032	23.65	5.11	<45	225	250	
PYX032	23.65	5.11	45–90	227	255	
PYX032	23.65	5.11	90–250	230	250	
PYX032	23.65	5.11	250–500	230	250	
PYX032	23.65	5.11	500–1000	225	255	
High-calcium pyroxenes (spectral type B)						
PYX018	2.42	0.00	<45	216	262	
PYX017	4.88	1.25	<45	223	267	
PYX034	5.21	2.03	<45	217	265	
PYX005	5.93	0.77	<45	220	253	
PYX036	8.18	1.71	<45	227	260	
PYX114	11.34	0.57	<45	222	251	
PYX101	12.99	1.44	<45	217	252	
High-calcium pyroxenes (spectral type A)						
PYX020	2.07	0.00	<45	223	272	
PYX150	2.56	0.00	<45	220	269	
PYX009	6.20	0.00	<45	215	272	
PYX010	10.18	4.83	<45	222	268	
PYX039	10.26	6.47	<45	225	272	
PYX038	17.49	8.70	<45	225	273	
PYX021	23.25	3.81	<45	225	277	

(*continued on next page*)

Table 3 (*continued*)

Mineral	wt% FeO	wt% Fe_2O_3	Grain size (μm)	Band minima (nm)	
Plagioclase feldspars[a]					
PLG103		0.03	<45	215	250
PLG105		0.07	<45	215	250
PLG106		0.07	<45	215	250
PLG115		0.07	<45	215	250
PLG120		0.14	<45	220	250
PLG104		0.41	<45	220	250
PLG130		0.42	<45	225	253
PLG130		0.42	45–90	223	250
PLG130		0.42	90–250	222	275
PLG130		0.42	250–500	222	270
PLG130		0.42	500–1000	225	273
PLG109		0.43	<45	225	250
PLG114		0.58	<45	225	250
PLG111		0.59	<45	225	250
PLG122		0.61	<45	225	250
PLG108		0.64	<45	225	255
Basalt[b]					
SA-51	14.23		<45	225	250
SA-51	14.23		45–90	225	250
SA-51	14.23		90–250	225	272
SA-51	14.23		250–500	225	270
SA-51	14.23		500–1000	225	272
Phyllosilicates					
CHM102	29.09	25.92	<45	230	
MON101	0.26	5.65	<45	225	260
NON101	0.79	22.08	<45	230	270
Sulfates					
SPT107	0.16	89.76	<45	262	340
SPT143	0.00	0.00	<45	230	
SPT207			<45	227	

[a] All Fe reported as Fe_2O_3.
[b] All Fe reported as FeO.

ture of these bands, and the unlikely occurrence of monomineralic exposures on planetary surfaces.

It would be useful to be able to determine band widths as a possible additional parameter for discriminating different minerals, as well as for constraining degree of crystallinity. However, the UV absorption bands in the 200–300 nm region invariably "appear" broad, and are superimposed on what is almost always a broad sloping continuum. There are also additional strong absorption features at even shorter wavelengths (Wagner et al., 1987). In addition, and as discussed above, many of the UV Fe–O absorption features may be saturated (Blazey, 1977). When all of these factors are coupled with the low overall reflectance in the UV, it is impossible to ascertain whether the sloping continuum is associated with the UV absorption features of interest and/or the shorter wavelength absorption features and how a continuum should be constructed to isolate the absorption features of interest. It seems likely that metal–oxygen charge transfers are inherently broad as metal–oxygen distances vary depending on site geometry, cation substitutions, degree of crystallinity, and other structural defects. The most comparable situation would be how crystal field transition bands become broader and less well-resolved as grain size increases (e.g., Hunt and Salisbury, 1970). In the UV region, band broadening due to saturation seems to occur at even the smallest grain sizes (<45 μm) for many Fe-bearing minerals.

7.1. Spectral changes associated with opaque phases

As discussed below, planetary spectroscopy often involves discussions of spectral slopes, with terms such as "red-sloped" and "blue-sloped" commonly used. Reflectance ratios are also often commonly used to discriminate differences in target properties (e.g., Robinson et al., 2007). The factors that will change spectral slopes are many, and a detailed discussion of all of them is outside the scope of this paper. The results of this study indicate that UV band saturation seems to affect many Fe-bearing minerals at even small grain sizes, Here we focus on the effects of opaque minerals on mafic silicate spectra.

As discussed above, overall spectral slopes of mafic silicates in the UV region are affected by factors such as Fe abundance and its oxidation state, and grain size. When opaques are present (such as ilmenite, meteoritic metal, or SMFe), their effect on spectral slope of the silicates with which they are associated will be a function of the grain size and abundance of the opaques, as well as the wavelengths used to define the spectral slope. Meteoritic metal is usually considered to be a "red-sloped" material when considered alongside mafic silicates. However in the 250–400 nm interval, the <45-μm sized meteoritic metal has a 400/250 nm reflectance ratio of 1.47. Contrast this with olivine: the 400/250 nm ratio for the <45 μm fraction of OLV003 (a typical low-iron olivine) is 4.57. Thus, over this interval, olivine is the more red-sloped phase. For a different wavelength interval and reflectance ratio (e.g., the 500–2500 nm interval), the 2500/500 nm ratio for the meteoritic metal and olivine is 1.52 vs 1.32, respectively, thus, over this interval, meteoritic metal is more "red-sloped."

When considering the spectrum-altering effects of opaque minerals, they need to be considered in the context of the other phases with which they are present (in addition to their abundance, grain size, and wavelength region of interest). Thus, there are many factors that will affect "spectral slope." In the case of SMFe and meteoritic iron, their spectra are flatter over the 200- to 400-nm interval than the silicates they are commonly associated with in lunar and meteoritic samples (pyroxene, olivine, plagioclase feldspar). The silicates exhibit their steep reflectance decline toward shorter wavelengths over this interval, where their spectral behavior changes from surface scatter-dominated at shorter wavelengths to volume scatter-dominated at longer wavelengths. By contrast, opaque minerals are dominated by surface scattering. Therefore when spectral slopes or ratios are used that straddle the silicate spectral dropoff, increasing opaques (whether ilmenite or meteoritic metal) will generally show a bluing effect. This may or may not be accompanied by a decrease in reflectance: ilmenite reflectance in the 200–400 nm region is higher than some of the mafic silicates used in this study. Therefore, the abundance of opaque minerals, and the spectral nature other minerals that they are associated with, will determine whether the spectrum of a mixture in which they are present is: red-sloped, how red-sloped, red-sloped over what interval, the wavelength position of the reflectance rise associated with the change in spectral slope, and the intensity of the reflectance rise.

8. UV planetary spectroscopy

In many remote sensing situations, reflectance data are acquired at discrete wavelengths rather than in contiguous band passes. This necessitates the use of different analytical tools, such as reflectance ratios, rather than absorption band positions, to attempt to constrain surface mineralogies. While a number of recent and upcoming planetary missions will be acquiring UV reflectance data across contiguous band passes, discrete band pass data is being, and will continue to be, widely used. We have examined a number of reflectance ratios that have been used in previous planetary remote sensing campaigns in order to ascertain the utility of reflectance ratios for planetary mapping based on UV data.

One factor worth noting in relation to reflectance ratios is that they can be affected by variations in a number of target properties. For the olivine and plagioclase grain size series, the 344/290 and 502/290 nm reflectance ratios (chosen for their utility for lunar surface mapping; Robinson et al., 2007) initially increase and then decrease with increasing grain size (Fig. 12a, Table 4). Changes in

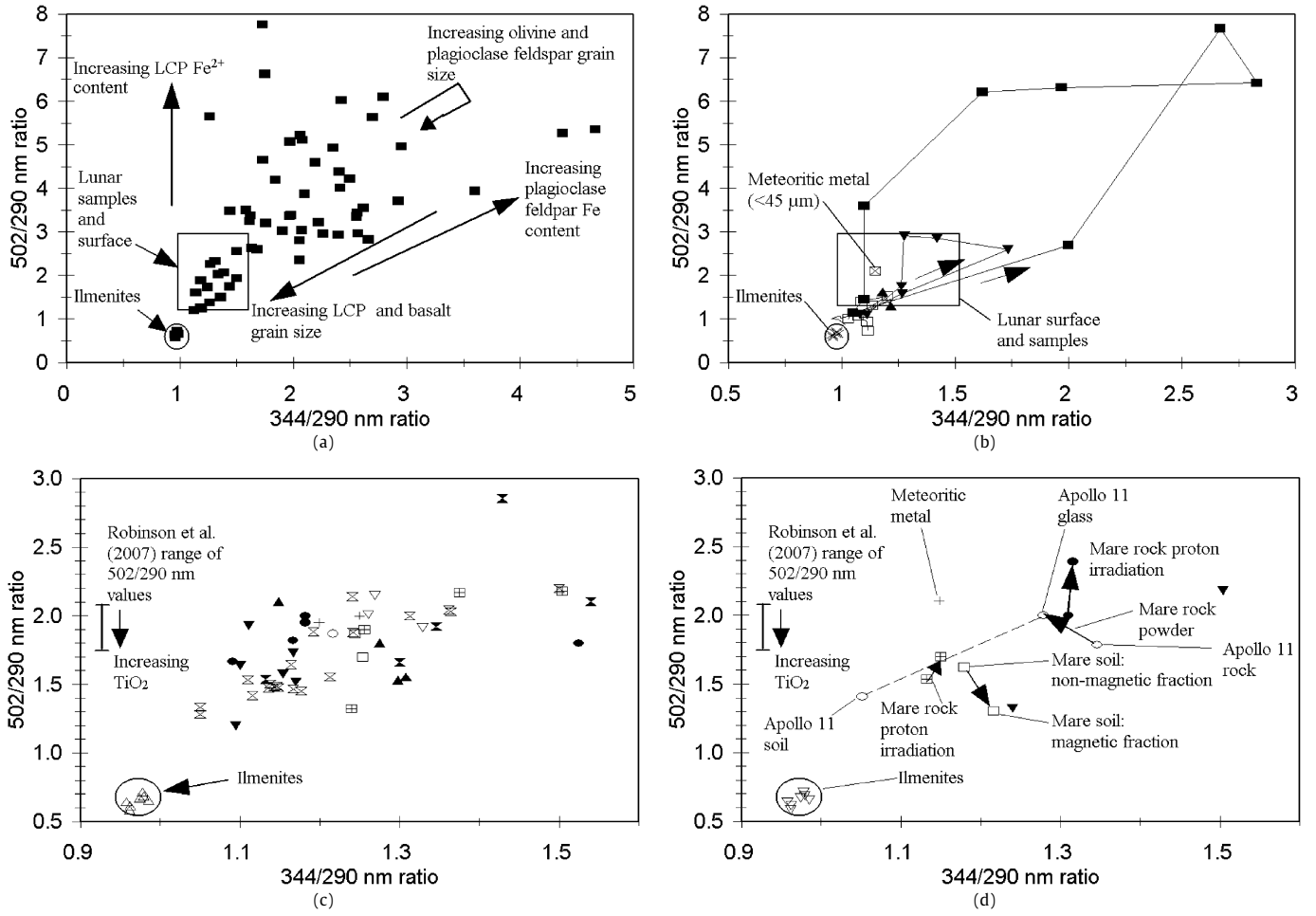

Fig. 12. (a) 502/290 versus 344/290 nm reflectance ratio for lunar analog minerals included in this study. The areas occupied by lunar surface and sample spectra are outlined. The direction of change in reflectance ratios for variations in various parameters are indicated by arrows. Increasing olivine and plagioclase grain sizes lead to an initial increase, followed by a decrease in reflectance ratios with progressively increasing grain size. (b) Same as panel (a) but showing the trends exhibited by the sample spectra of Noble et al. (2007). The areas occupied by ilmenites and lunar surface and sample spectra, and the point for meteoritic metal are also indicated. The arrows indicate the trajectories in reflectance ratios for the two smallest grain size series of Noble et al. (2007). Reflectance values at 300 nm rather than 290 nm were used for the Noble et al. (2007) ratios because of a lack of data below 300 nm. Note change of scale from panel (a). (c) Same as panel (a) for lunar samples. Symbols and sources of data: filled square: immature mare soils (Noble et al., 2001); filled circle: submature mare soils (Wagner et al., 1987; Noble et al., 2001); filled downward triangle: mature mare soils (Conel and Nash, 1970; Hapke, 2001; Noble et al., 2001); open square: immature highland soils (Noble et al., 2001); open circle: submature mare soils (Noble et al., 2001); open downward triangle: mature highland soils (Wagner et al., 1987; Noble et al., 2001); cross: lunar surface (Lucke et al., 1973, 1976); filled hourglass: mare rocks (Conel and Nash, 1970; Wagner et al., 1987; Hapke, 2001); open circle and cross: highland rocks (Wagner et al., 1987); open hourglass: mare soils (Nash and Conel, 1971; Antipova-Karataeva et al., 1973; Hua et al., 1976; Wagner et al., 1987); open upright triangle: highland soils (Hua et al., 1976); X: ilmenites (this study); –: meteoritic metal (this study). (d) Same as panel (a) for various "treatments"; filled square: irradiated mare rock (Conel and Nash, 1970); filled circle: irradiated mare rock (Hapke, 2001); open square: magnetic vs non-magnetic mare soil (Hapke, 2001); open circle: Apollo 11 rock vs glass vs soil (Hapke, 2001); X: ilmenites (this study); –: meteoritic metal (this study).

the direction of reflectance ratio variations are due to the competing effects of decreasing overall reflectance with increasing grain size and absorption band saturation. Initially overall reflectance decreases as grain size increases and absorption bands become deeper. The increase in band depth is greater than the decrease in overall reflectance and the 344/290 and 502/290 nm reflectance ratios are a rough measure of the depth of the Fe^{2+}–O charge transfer band located near 270 nm.

As grain size further increases, the main absorption band becomes saturated, and as a result reflectance in the area of saturation decreases only very gradually, if at all, with further increases in grain size. However reflectance continues to decrease with increasing grain size outside the area of saturation. The absorption band appears to become wider with an increasingly broad flat bottom. Reflectance ratios based on a value at a wavelength outside the area of saturation (e.g., 502 nm) to a value at a wavelength inside the area of saturation (e.g., 290 nm) will consequently begin to decrease as the 502 nm value continues to decrease and the 290 nm value is essentially constant or decreasing less rapidly. The point at which a band becomes saturated is a function of the competing effects of surface versus volume scattering.

Reversals in the direction of change in reflectance ratios are also seen for nanophase iron embedded in silica gels (Fig. 12b; Noble et al., 2007). In this case, the variations in reflectance ratio are a function of both the abundance and size of the nanophase iron particles. All but the largest size (50 nm) of the nanophase particle runs exhibit initial increases in 344/290 and 502/290 nm reflectance ratios followed by a decrease, with the most abundant end point having reflectance ratios similar to the lowest abundance starting point, but with significantly lower overall reflectance. These results show that the degree of reddening is a function of both abundance and size of nanophase iron particles. The dramatic changes in reflectance ratios are likely larger than the changes that would occur on planetary surfaces, where any nanophase iron particles are mixed with various minerals that are also relatively dark in the UV.

Table 4
Changes in 344/290 and 502/290 nm reflectance ratios as a function of various parameters

Parameter	344/290 nm ratio	502/290 nm ratio
Increasing ilmenite grain size	No significant change	No significant change
Increasing olivine Fe content	No systematic change	No systematic change
Increasing olivine grain size	Increase, then decrease	Increase, then decrease
Increasing plagioclase Fe content	Increases	Increases
Increasing plagioclase grain size	Increase, then decrease	Increase, then decrease
Increasing HCP Fe^{2+} content	No systematic change	No systematic change
Increasing LCP Fe^{2+} content	No systematic change	Increases
Increasing LCP grain size	Decreases	Decreases
Increasing basalt grain size	Decreases	Decreases
Increasing maturity—mare soils	Increases	Decreases
Increasing maturity—highland soils	No systematic change	Increases
Rock vitrification	Decreases	Increases
Proton irradiation	Increases	Increases
Magnetic fraction vs bulk soil	Possibly redder	Redder
Increasing TiO_2/ilmenite content	Decreases	Decreases

8.1. Lunar UV spectral properties

The ultraviolet spectral reflectance properties of the Moon have been investigated by a number of groups using various instruments and platforms. Lebedinsky et al. (1967a, 1967b, 1968) presented spectra acquired over various parts of the lunar surface by the Zond 3 space probe. The instrument provided data from 190 to 350 nm with a spectral resolution of between 1.3 and 1.5 nm. Data were presented over the ranges 190–275 nm (15 spectra; Lebedinsky et al., 1967a), and 285–355 nm (unknown number of spectra; Lebedinsky et al., 1967b). The averaged data show a decrease in average albedo from ~4% at 355 nm to 3% at 340 nm, a generally flat spectrum from 340 to 310 nm, followed by a more abrupt decrease in reflectance from 310 to 285 nm (~1% reflectance). Lebedinsky et al. (1967a) suggested that albedo variations present in the visible spectral region for different regions on the Moon persist into, and are accentuated in, the UV. Their 190 to 270 nm data suggests a reflectance maximum near 240 nm (~2% reflectance) and generally decreasing reflectance toward both shorter and longer wavelengths (~1% reflectance at 200 and 175 nm). There is also fine structure superimposed on the spectrum which was not discussed. Further discussion of the data (Lebedinsky et al., 1968) suggests that there exists a sharp increase in brightness over the range 242 to 247 nm that, for the lunar farside, they attribute to some form of luminescence.

Carver et al. (1974) presented whole disk spectra of the Moon obtained in a series of rocket flights, covering the range from 240 to 290 nm, and compared their results to previous investigations. They found that the lunar albedo drops sharply from the visible region toward shorter wavelengths, dropping by a factor of ~10 to ~0.7% at 240 nm. Their results, obtained at selected wavelengths, suggest a reflectance minimum of ~0.5% near 260 nm, and a slight rise toward 240 nm (to ~0.8%).

Lucke et al. (1973, 1976) present combined ultraviolet lunar albedo measurements obtained by previous investigators (for comparison with lunar samples and Apollo 17 results). Their compendiums suggest that overall lunar albedo decreases from ~7% at 400 nm to a minimum near 200–220 nm of ~4%. They also critically intercompare the results of previous investigators, finding that large discrepancies in absolute values exist between many of the previous investigations. In spite of these discrepancies, they stated that a decline in lunar albedo toward shorter wavelengths over the 200 to 400 nm range is well established.

Stair and Johnson (1953) acquired whole disk lunar spectra over the range 320–550 nm. They found that the lunar spectra exhibited an absorption feature from 380–390 nm and a steep dropoff in reflectance from 360 to 320 nm. Based on the results of our study, it seems likely that the 380–390 nm band is attributable to the Fe^{2+}–O charge transfer in plagioclase feldspar.

Overall, previous lunar UV observations of large areas suggest that reflectance declines toward shorter wavelengths. The absorption feature near 340 nm is best attributed to ilmenite. The additional absorption features near 200–220 and 285 nm can plausibly be attributed to a number of silicate minerals, including plagioclase feldspar, and are not particularly diagnostic of any one mineral.

More recently, higher spatial resolution studies of the Moon have been undertaken using Earth- and space-based telescopes, and spacecraft. These observations have been performed at discrete band passes. A number of investigators have developed various techniques to derive lunar TiO_2 abundances from these and older multispectral observations, as well as to separate the effects of increasing maturity, FeO content, and highlands versus mare. It should be emphasized that lunar rocks and soils are highly reduced and are essentially devoid of Fe^{3+} (Heiken et al., 1991). Hence, the use of terrestrial samples, which almost invariably contain some Fe^{3+}, for analysis of lunar spectra should be undertaken cautiously.

To better illustrate the ensuing discussion and derived relationships, the 200–860 nm spectra of our ilmenites are shown in Figs. 3g and 3i. Charette et al. (1974) examined both lunar samples and telescopic spectra to derive a relationship between spectral parameters, maturity and TiO_2 content. They found that the spectral slope from 402 to 564 nm increases with increasing maturity and TiO_2 content. When combined with the 564/948 nm reflectance ratio, discrimination between major surface units was possible. Subsequent to its development, these relationships were used extensively to map TiO_2 concentrations across the lunar surface (e.g., Melendrez et al., 1994).

Blewett et al. (1997) applied Clementine multispectral data to lunar TiO_2 mapping. They found that for various Apollo mare sites, the 415/750 nm reflectance ratio increases with increasing TiO_2 concentration while absolute reflectance at 750 nm decreased. For highland sites, the 415/750 nm ratio also decreased with increasing TiO_2, while reflectance at 750 nm increased. This model was further refined in Lucey et al. (1998, 2000) in order to better account for FeO content variations and maturity. With the availability of Lunar Prospector data, discrepancies were found with the Clementine-derived Ti values, by up to a factor of two in some areas (Elphic et al., 2002). The earlier algorithm of Lucey and coworkers was subsequently modified (Gillis et al., 2003) to produce a better fit between the spectroscopic and neutron spectrometer data. Our laboratory spectral data indicates that the 415/750 nm ratio provides partial separation between ilmenites and our other samples. Ilmenites have 415/750 nm ratios of between 0.94 and 1.02. The majority of the plausible lunar minerals have ratios >1.02 with the exception of one low-calcium, one high-calcium pyroxene, and the largest grain sizes of the olivines (250–500 and 500–1000 μm). Some of the pure plagioclase spectra also have 415/750 nm ratios close to 1.02.

Robinson et al. (2006, 2007) and Garvin et al. (2006) acquired Hubble Space Telescope (HST) images of the Moon through four filters, centered at ~290, 344, 502, and 658 nm, in order to determine whether UV observations can be used to constrain lunar surface TiO_2 abundances. Their analysis suggests that the 502/290 nm reflectance ratio is negatively correlated with TiO_2 abundance, and that reflectance variations exist in the UV that can be used to delineate different geologic units. Robinson et al. (2007) examined additional reflectance ratios for discriminating maturity from compositional variations. They found that the 502/290 nm reflectance ratio is useful in this regard, as this ratio is more sensitive to TiO_2 abundance than maturity. Our current data support this notion (Fig. 12c). Ilmenite is spectrally flat to blue-sloped across the 250–500 nm interval, while the constituent minerals and submi-

croscopic iron (SMFe) are red-sloped across the same interval. As a result, ilmenite has lower 344/290 and 502/290 nm ratios than any lunar samples, and Robinson et al. (2007) found that increasing TiO_2 content causes the 502/290 nm ratio to approach the pure ilmenite values.

We examined all possible reflectance ratios of the HST filters and found that discrimination of ilmenite from other lunar minerals must utilize one of the short wavelength bands: either the 290 or 344 nm band. However, again as a cautionary note, most of our terrestrial analogues contain detectable levels of Fe^{3+}, and hence may not be suitable lunar analogues. However, decreasing Fe^{3+} content generally leads to increases in longer-to-shorter wavelength reflectance ratios, hence discrimination of ilmenite from other lunar minerals would be enhanced over the terrestrial case. The minerals that are closest to ilmenite for the various reflectance ratios vary somewhat for different reflectance ratio. Plagioclase feldspar is generally the most similar to ilmenite in terms of reflectance ratios; this is due to its low Fe content which translates into a flatter reflectance spectrum than the other Fe-bearing minerals. The spectral uniqueness of ilmenite (blue sloped between ~200 and 500 nm) versus other common lunar minerals (red sloped between ~200 and 500 nm) was also noted by Robinson et al. (2007). It is also worth noting that ilmenite is not the only lunar oxide. Other known lunar oxides include spinels occupying the compositional space between chromite ($FeCr_2O_4$), ulvöspinel (Fe_2TiO_4), and hercynite ($FeAl_2O_4$), as well as armalcolite ($FeTi_2O_5$–$MgTi_2O_5$) (Papike et al., 1976; Stanin and Taylor, 1979; Mulcahy et al., 2004), and they can make up as much as 10% of the volume of some basalt samples (Papike et al., 1991). These materials exhibit diverse spectral shapes, particularly in the UV–vis region (Riner et al., 2005); consequently the selection of discrete band passes for their detection or discrimination should be undertaken with the goal of maximizing these differences, and may vary for different oxides.

The 502/290 and 344/290 nm reflectance ratios for the plausible lunar minerals included in this study are shown in Fig. 12a. Available lunar sample and surface spectra occupy only a small portion of the full range covered by the minerals used in this study. How changes in various target properties affect these ratios are shown in Fig. 12a and listed in Table 4. As noted by Robinson et al. (2007), the Clementine 750/415 nm ratio does not provide adequate discrimination between the spectrum-altering effects of ilmenite from other factors. This observation verifies that the spectral properties of ilmenite in the UV differ from other lunar materials, and that the UV region is the most useful for mapping TiO_2-rich materials (Robinson et al., 2007).

A similar analysis was performed for the Lunar Reconnaissance Orbiter camera (LROC) band passes. LROC will image the lunar surface through seven filters centered at 315, 360, 415, 560, 600, 640, and 680 nm (Chin et al., 2007). Examination of all possible two-filter reflectance ratios indicates that all of the combinations involving at least one of the 315, 360, and 415 nm filters can fully discriminate pure ilmenite from all of the other minerals in this study (we used only single channel reflectance ratios for this examination, and did not attempt to convolve the laboratory data to the transmission curves of the LROC filters). This result mirrors that found for the HST filters discussed above.

A common assumption in lunar spectroscopy is that increasing maturity results in lower albedo and an overall reddening of spectral slopes (e.g., Hapke, 2001). Lunar soils are darker than powdered rock spectra of similar compositions, and non-magnetic fractions are brighter than the magnetic fractions of bulk soils and the bulk soils themselves (e.g., Adams and McCord, 1973; Wagner et al., 1987; Hapke, 2001) (Table 5). Magnetic fractions are more red-sloped than bulk soils over the 500–2500 nm range (Adams and McCord, 1973) (Table 5). Overall spectral slopes (using the 2500/500 nm reflectance ratio) are also generally redder with increasing maturity for both mare and highland soils (Noble et al., 2001). However the situation is different in the UV–vis region, and this has been noted by a number of investigators for the Moon and other planetary bodies (e.g., Hendrix and Vilas, 2006, and references therein). Spectral slopes in this region, measured by the 500/300 or 500/350 nm nm reflectance ratio, generally decrease with increasing maturity for mare samples but increase with increasing maturity for highland samples (Table 5). Thus, when discussing changes in spectral slope, the relevant wavelength interval over which a relationship applies must be specified.

Table 5
Reflectance ratios for selected lunar samples

Sample ID and type	Reflectance ratios (nm)		Source of data
	500/350	2500/500	
67461 soil, bulk sample	1.30	1.80	[1]
67461 soil, non-magnetic fraction	1.40	1.69	[1]
67461 soil, magnetic fraction	1.38	2.21	[1]
68841 soil, bulk sample	2.57	4.21	[1]
68841 soil, non-magnetic fraction	1.98	2.80	[1]
68841 soil, magnetic fraction	2.23	4.47	[1]
67455 white breccia, <250 μm	1.37	1.44	[1]
60016 dark breccia, <250 μm	1.25	1.34	[1]
68815 dark breccia, <250 μm	1.25	1.49	[1]
60601 mature soil	1.64	3.22	[1]
	500/300	2500/500	
12030,14: immature mare soil, <10 μm	2.16	2.47	[2]
71061,14: immature mare soil, <10 μm	1.95	3.49	[2]
12001,56: submature mare soil, <10 μm	1.86	3.85	[2]
15071,52: submature mare soil, <10 μm	2.17	3.97	[2]
70181,47: submature mare soil, <10 μm	1.91	3.81	[2]
71501,35: submature mare soil, <10 μm	1.95	3.66	[2]
10084,78: mature mare soil, <10 μm	1.64	3.50	[2]
15041,94: mature mare soil, <10 μm	2.07	4.14	[2]
79221,81: mature mare soil, <10 μm	1.75	3.82	[2]
14141,07: immature highland soil, <10 μm	2.05	1.92	[2]
61221,92: immature highland soil, <10 μm	1.74	1.44	[2]
67461,25: immature highland soil, <10 μm	1.82	1.74	[2]
67701,39: submature highland soil, <10 μm	1.90	1.65	[2]
14163,57: mature highland soil, <10 μm	1.93	2.84	[2]
14259,85: mature highland soil, <10 μm	2.17	3.66	[2]
14260,07: mature highland soil, <10 μm	1.98	3.96	[2]
62231,91: mature highland soil, <10 μm	1.78	2.82	[2]
64801,71: mature highland soil, <10 μm	2.08	2.27	[2]
68501,85: mature highland soil, <10 μm	1.98	2.99	[2]

Source of data: [1] Adams and McCord (1973). [2] Noble et al. (2001).

Another parameter that has been used to describe lunar sample spectra, particularly in the UV, is “turnover” (Lucke et al., 1974; Wagner et al., 1987; Hendrix and Vilas, 2006). This refers to a reversal in absolute reflectance, whereby spectra that are lighter in the visible and near-infrared are darker in the far-UV. For the Moon, this turnover generally occurs shortward of 200 nm and hence is applicable only to analysis of data that extends to below 200 nm (Hapke et al., 1978; Wagner et al., 1987). Vesta exhibits a hemispheric spectral reversal; in this case the reversal occurs near 250 nm (Hendrix et al., 2003).

The effects of various lunar sample properties and alteration processes on reflectance ratios are shown in Fig. 12d and listed in Tables 4 and 5. Increasing maturity in mare soils leads to an increase in 344/290 nm ratio and a decrease in the 502/290 nm ratio, while in highland soils, the 502/290 nm ratio increases (Noble et al., 2007). The trends are not absolute for every sample because lunar soil samples are not well-constrained assemblages. In addition, the spectral properties of SMFe, which likely account for most of the spectral variation between different maturity classes (Hapke, 2001), are a complex function of particle size and abundance (Noble et al., 2007). Both the 344/300 and 502/300 nm reflectance ratios increase for a given wt% of SMFe, as the size of

Table 6
344/300 and 502/300 nm reflectance ratios of "submicron" Fe^0 (From Noble et al., 2007)

Grain size (nm)	Abundance wt%	Reflectance ratio	
		344/300 nm	502/290 nm
2	0.54	1.62	6.21
6	0.30	1.26	1.75
25	0.58	1.07	1.07
50	0.50	0.99	0.99

the particles is reduced (Table 6). At sizes and abundances appropriate to lunar soils (generally < a few nanometers and ~0.5 wt%; Morris, 1980; Noble et al., 2007), Fe particles would strongly redden the 502/290 nm ratio, more so than the 344/290 nm ratio (Table 6).

Other lunar surface modification processes have variable effects on UV and visible spectra. Vitrification seems to lead to an increase in 502/290 nm ratio and a decrease in 344/290 nm ratio (Hapke, 2001). By contrast, proton irradiation leads to increases in both ratios (Conel and Nash, 1970; Hapke, 2001). The magnetic fraction of soils is redder as measured by the 502/290 nm ratio compared to bulk soils (Hapke, 2001). Increasing TiO_2/ilmenite concentration results in decreases in both reflectance ratios, attributable to the blue-sloped spectrum of ilmenite across this wavelength region.

The main alteration mechanisms accompanying maturity are the production of glass, a greater fraction of finer-grained minerals, and SMFe (Hapke, 2001). Each of these processes will lead to spectral changes. The production of glass causes a broadening of absorption bands; in the UV, minerals generally exhibit a steep reflectance rise in the 300–400 nm region due to metal–O charge transfers. With vitrification, the mineral structure is disrupted, and while metal–O charge transfers still occur, they are spread out across a greater range of wavelengths and the steep reflectance rise becomes more gradual (Hapke, 2001). Reflectance ratios may increase or decrease depending on the wavelength values used and how the reflectance rise is modified. In the case of the single reliable lunar vitrification experiment (Hapke, 2001), vitrification reduced the 344/290 nm ratio and increased the 502/290 nm ratio.

Ion irradiation of powders leads to darkening of Fe-bearing targets due to deposition of Fe. Both the 502/290 and 344/290 nm reflectance ratios increase after irradiation (Conel and Nash, 1970; Hapke, 2001). The mechanism by which ion-induced sputtering causes these spectral changes is likely due to the formation of SMFe (Hapke, 2001). SMFe is more red-sloped than fine-grained constituent lunar minerals (compare reflectance ratios in Figs. 12a and 12b) over the 300–500 nm interval at abundances appropriate to mature lunar samples (~0.5 wt% SMFe). The spectral reddening due to SMFe formation is supported by the fact that the magnetic fractions of lunar soils have higher reflectance ratios than the bulk soils (Table 5). The reflectance spectra of mare soils suggest that the 502/290 nm ratio decreases with increasing maturity (Noble et al., 2001), opposite the trend found for irradiation. However spectral differences between different soil samples could also be attributed to other factors such as differences in mineralogy or ilmenite abundances. Highland soils exhibit the expected increase in 502/290 nm ratio with increasing maturity. Collectively, these results suggest that measuring differences in ilmenite abundance using optical spectroscopy requires the use of UV wavelengths.

8.2. Asteroid UV spectral properties

UV spectroscopic studies of S-class asteroids show some similarities to lunar mare soils, in that increasing space exposure leads to an overall reduction in spectral slope in the 300–400 nm region (Hendrix and Vilas, 2006). Comparison of the reflectance spectra of SMFe (Noble et al., 2003) and meteoritic metal (this study) shows that the 400:300 nm reflectance ratio of these materials is ~1.2 for meteoritic metals (for various grain sizes), and can be lower than this value for SMFe. The reflectance ratio for common constituent minerals (mafic silicates) is $\gtrsim$1.5, indicating that the accumulation of SMFe (or enhanced concentrations of meteoritic metal) on asteroid surfaces would lead to a reduction in this reflectance ratio. The longer wavelength reddening that is seen with increasing space exposure, as measured by the 1640:550 nm reflectance ratio (Hendrix and Vilas, 2006) is also consistent with enhanced metal abundances. Meteoritic metal has a 1640:550 nm ratio of ~1.45, whereas common meteoritic mafic silicates (olivine, LCP, HCP) have reflectance ratios <1.45 regardless of their iron content or grain size.

8.3. Mercury UV spectral properties

The MESSENGER spacecraft, which first encountered Mercury in early 2008 (flyby) and will settle into orbit around the planet in 2011, carries a UV–vis spectrometer (MASCS) that will cover the 115–600 nm region with 0.5–1.0 nm spectral resolution (Gold et al., 2001). By analogy with the Moon, it is likely that the UV spectral region will be particularly useful for identifying areas containing various abundances of metal oxides. Current data suggest variable surface composition and opaque abundances, and a generally Fe-poor surface (Robinson and Lucey, 1997; Robinson and Taylor, 2001; Blewett et al., 1997, 2007; Warell, 2003; Warell and Blewett, 2004). More specific spectral interpretations include evidence for the presence of Fe-bearing high-Ca pyroxene (Warell et al., 2006), sulfur, iron-bearing sulfides (Sprague et al., 1995), nepheline-bearing alkali syenite, and plagioclase feldspar–pyroxene mixtures (Sprague and Roush, 1998; Warell, 2003), intermediate SiO_2 content materials and clinopyroxene (Sprague et al., 2002), and intermediate, mafic, and ultramafic rock types (Cooper et al., 2001) across some parts of the surface. Opaque abundances are likely lower than on the lunar surface, but may be comparable to the most anorthositic lunar highlands (Blewett et al., 2002; Warell and Blewett, 2004). By analogy with the Moon, the UV data should provide a means for discriminating opaque abundance variations. Data from the spring 2008 flyby provided usable data only across the 170–320 nm range (Vilas et al., 2008).

8.4. Mars UV spectral properties

The UV spectral reflectance properties of Mars have been measured using HST (Bell et al., 1997; Bell and Ansty, 2007). The main purpose of Bell et al. (1997) was to determine whether UV data could be used to provide some insights into surface mineralogy. We analyzed our laboratory data using the band passes of Bell et al. (1997) to determine whether hematite and other oxides and hydroxides can be discriminated from other martian minerals. We have found that pure hematite, regardless of grain size, can be discriminated from the other minerals included in this study (except ilmenite) on the basis of UV reflectance ratios, specifically the 333/256, 409/256, and 501/256 nm ratios. Fig. 13 shows the UV reflectance ratios that provide the best discrimination of hematite from the other minerals in this study. Hematite, up to grain sizes of 500–1000 μm, can be reliably discriminated from other minerals in this study. These results suggest that UV spectroscopy could potentially be applied to detection of hematite-rich areas on Mars, complementing the results obtained from the thermal IR (e.g., Christensen et al., 2001). The areas occupied by Mars bright and dark regions (Bell et al., 1997) are also shown in Fig. 13. The areas occupied by the reflectance ratios for the dark regions are slightly closer to the pure hematite "end point" than the bright regions. This suggests that at least some of the dark regions are

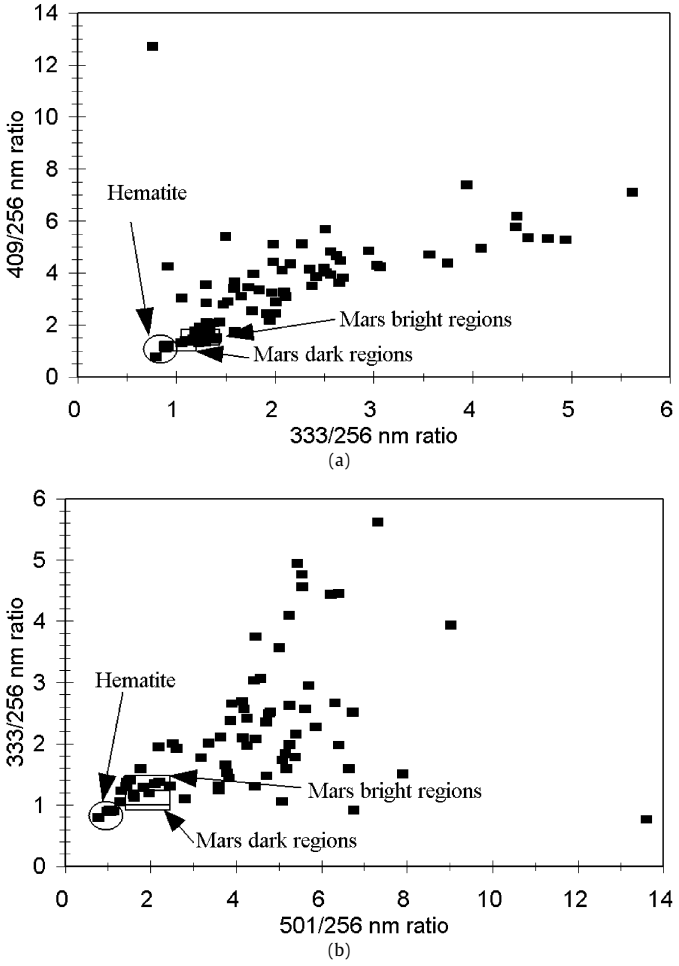

Fig. 13. Reflectance ratios for the samples used in this study, except ilmenite. (a) 409/256 vs 333/256 nm; (b) 333/256 vs 501/256 nm. The areas occupied by the hematites (all grain sizes), and telescopic spectra of Mars bright and dark regions (Bell et al., 1997) are indicated.

more hematite rich than bright regions (Bell et al., 1997). There are a number of past and current instruments on Mars orbiters that could potentially be used for UV observations of the martian surface, including SPICAM on Mars Express, MARCI on MRO, and the Mariner ultraviolet spectroscopy experiment (Hord et al., 1970; Barth and Hord, 1971; Bertaux et al., 2006; Malin, 2006).

9. Summary and conclusions

The UV spectral reflectance properties of various geological materials are dominated by the particular transition series elements that are present. For the inner Solar System and common rock-forming minerals, the most important of these are Fe^{3+}, Fe^{2+}, and Ti^{4+}. The presence of these elements leads to the appearance of metal–O charge transfer bands. These bands are generally broad and intense, with Fe^{3+}–O bands being particularly intense. The intensity of metal–O charge transfer bands is a function of numerous factors, such as abundance of the absorbing species and grain size. The position of metal–O charge transfer bands is a function of the type of absorbing species, the coordination environment, and the intensity of the band and adjacent absorption bands (due to overlapping absorptions and band saturation effects).

In spite of the various complicating factors that largely preclude the use of UV absorption bands for mineral identification, UV absorption bands can be used to identify the presence of specific transition series metals, even at low concentrations. The dominance of Fe in the UV spectra of plagioclase feldspars, in spite of low Fe abundances (<1%) is a case in point. In selected case, it may be possible to identify the presence of specific mineral species, provided these species are present in spectrally detectable amounts and any spectral interferences from other species can be accounted for. A few minerals, most importantly ilmenite, may be spectrally detectable through their unique spectral slopes in the UV, rather than solely on the basis of absorption band wavelength positions.

This study has also shown that the UV spectral properties of most minerals are dominated by effects other than those associated with longer wavelength spectral behavior. For common rock-forming minerals, diagnostic spectral properties in the visible–near infrared (400–2500 nm) region are largely affected by crystal-field transitions, metal–metal charge transfers, and overtones and combinations of various longer wavelength vibrational/rotational bands. The UV, by contrast is dominated by metal–O charge transfers. Absorption bands in this region can serve as a very sensitive indicator of the presence of even trace amounts (<0.01%) of some transition series elements, such as Fe^{3+}. However, this high sensitivity is accompanied by factors that can complicate mineral identification, including overlaps between band positions for most common rock-forming minerals, and rapid saturation of absorption bands, leading to shifts in band positions that are not diagnostic of a particular mineral.

For planetary surface mapping based on discrete rather than contiguous bandpasses, it is important that the band passes be selected so that spectral differences between targets or materials of interest are maximized. Such studies are capable of addressing very specific questions concerning planetary surface composition.

Given that UV spectrometers capable of targeting planetary surfaces are being, and will continue to be, flown, the prospects for utilizing such data for specific surface mapping applications are promising. The types of questions that can be addressed rely on a knowledge of the spectral properties of potential target materials. It appears that UV spectroscopy can be used to derive surface composition information that may be unattainable in other wavelength regions, and hence is a valuable complement to other optical spectrometers.

Acknowledgments

Thanks to Sarah Noble for providing some of the lunar sample spectra used in this analysis. The laboratory spectral measurements were made possible through the design and fabrication skills of Gundars Reinfelds, Joel Smigelski, and Harald Weigeldt of the University of Winnipeg. The kind assistance of Dr. Jeffrey Post (Smithsonian Institution National Museum of Natural History), Dr. Ted Roush (NASA Ames), Dr. Dick Morris (NASA JSC), Ms. Susan Atkinson (University of Alberta), and Mr. George Fulford (Alcan International) is gratefully acknowledged for their provision of some of the samples used in this study. We also wish to thank the following individuals for providing X-ray fluorescence, wet chemistry, and X-ray diffraction characterization of the samples used in this study: Ed Ghent and John Machacek (University of Calgary), Diane Caird (University of Alberta), and Frank Hawthorne and Neil Ball (University of Manitoba). Special thanks to Greg Gamble and Greg DeValentin of Gamble Technologies for their assistance and guidance in optimizing the performance and use of the Ocean Optics spectrometer. The Planetary Spectrophotometer Facility/HOSERLab, where this work was conducted, was established with funding from the Canada Foundation for Innovation, the Manitoba Research and Innovation Fund and the Canadian Space Agency. This study was supported by research grants and contracts from the Natural Sciences and Engineering Research Council of Canada (NSERC), the Canadian Space Agency, and the University of Winnipeg. Finally,

special thanks to Bruce Hapke and Faith Vilas for their many useful comments and suggestions, and their stamina in reviewing this manuscript.

Appendix A. Summary of previous UV laboratory observations

A.1. Greenman et al. (1967)

Greenman et al. (1967) measured reflectance spectra over the 200 to 300 nm range of a number of terrestrial rocks. Measurements were made with two systems: a Cary model 14 spectrophotometer equipped with a reflectance attachment; and a Tropel instrument. For the Cary measurements, the incident monochromatic beam was directed alternately to the sample and a standard with normal incidence. The reflected light was gathered by an integrating sphere and the absolute reflectance calculated as the ratio of the two signals. Slit width was adjusted automatically to maintain a constant intensity. Spectral resolution was on the order of 0.2–0.3 nm between 230 and 300 nm, and up to 1 nm for the 200 to 230 nm range. Magnesium carbonate ($MgCO_3$) was used as a reflectance standard. Its "absolute" reflectance was determined by comparison to freshly prepared MgO. Reflectance values for MgO were only available to as low as 240 nm and values to 200 nm were extrapolated from the available data.

The Tropel instrument consisted of a grating monochromator with a reflectometer mounted at the exit slit. The sample was mounted vertically in the reflectometer and could be rotated about a vertical axis to vary the angle of incidence or moved out of the light path to allow the incident light to be measured directly. The detector consisted of a sodium salicylate-coated glass light pipe leading to a photomultiplier tube. This could be rotated in a horizontal plane to vary the angle of detection or to measure the incident beam when the sample was withdrawn. The spectral resolution of this instrument was ~1 nm. The light pipe was partially masked, resulting in different collection efficiencies for the various configurations. For both the Cary and Tropel measurements, quartz cover plates were used on both samples and standards to hold the materials in place in the vertically mounted sample holders. There are a number of issues associated with this study: absolute reflectance values for the Tropel instrument are not reliable, as masking was used on some measurements. The uncertainty in the absolute reflectance of $MgCO_3$, especially below 240 nm also leads to uncertainties in absolute reflectance at shorter wavelengths.

A.2. Antipova-Karataeva et al. (1973)

Antipova-Karataeva et al. (1973) measured absorption and reflectance spectra of lunar samples, including large (8 mm × 8 mm) and small, essentially monomineralic (2 mm × 2 mm), spots. Absorption spectra were measured between 340 and 2400 nm on thin sections using a Hitachi Model EPS-3T spectrophotometer. Measurements were made relative to air or to the section holder. The section holder background spectrum was calculated and removed. Diffuse reflectance spectra were measured between 230 and 1800 nm relative to an MgO smoke standard. All of the lunar breccia samples showed reflectance increasing relatively smoothly toward longer wavelengths over the 200 to 400 nm interval. Absolute reflectance at 400 nm ranged between 3 and 8%.

This study did not provide enough details on the experimental procedures to fully evaluate its utility. For the transmission measurements, the effect of the section holder on the transmission spectra (whether it was present in both the background and sample measurements, and its composition) is unclear. The lunar samples also likely are not monomineralic at the spatial scale employed, so the spectra probably contain contributions from multiple phases. The use of MgO smoke as a standard may also introduce spectral artifacts, as its UV reflectance can be affected by a number of factors (e.g., Commission Internationale de L'Eclairage, 1979).

A.3. "Cohen group" (1974–1980)

Cohen and co-investigators presented a very comprehensive overview of UV reflectance spectra (from 90 to 248 nm) of various meteorites and other geological materials in a series of publications (Cohen et al., 1978; Hapke et al., 1978; Wagner et al., 1980, 1979; Wagner, 1980). The measurements were made in vacuum using a Jarrell-Ash monochromator light source, with the incident light being focused onto either the detector or the sample. Spectral resolution was on the order of 10 nm. The detector consisted of a light pipe with a fluorescent sodium salicylate coating on one end and with the other end optically coupled to a photomultiplier tube. The light pipe and sample could be rotated so that the detector looked either directly at the incident beam (as the standard) or at light scattered from the sample in a specular geometry with a phase angle of ~15°. They acknowledged that the viewing geometry only allows for absolute reflectance of specular surfaces to be obtained. They also noted that fluorescence from some minerals may introduce spurious spectral features.

Possible issues associated with these studies include the fact that the use of monochromatic incident light does not replicate actual planetary observations as well as a broadband incident light source with a wavelength-selective detector. In addition, the fluorescence of the salicylicide detector may be affected by the energy distribution of the reflected light from the sample, which may itself fluoresce.

A.4. Carver et al. (1975)

Carver et al. (1975) measured reflectance spectra of a number of terrestrial rock types. Spectra were acquired for rock slabs that had been polished with grinding powders ranging in size from 3 to 60 μm. They reported results largely for the samples ground with 60-μm sized powders. A McPherson vacuum UV monochromator equipped with a specially designed reflectometer was used for measurements over the 80–400 nm range, and provided a spectral resolution of approximately 1 nm. The reflectance "standard" measurements were made by directing the incident radiation directly onto the detector with no intervening optical elements. Sample measurements were made with the sample placed in the optical path of the incident monochromatic radiation and the detector rotated at some angle relative to the sample surface to intercept a portion of the reflected light. A Perkin–Elmer system was used for reflectance measurements over the 200–800 nm range, and operated in a specular bidirectional mode. The incident light illuminated a mirror (type unknown) as the standard or the rock surface as the sample, likely located in the same position as the mirror. The measured angular distribution function was used to calculate absolute albedos of the samples. The rock and mineral samples showed significant variations in spectral properties.

The use of the incident beam directed directly at the detector as the standard versus bidirectional or specular light reflected off the samples made determination of absolute reflectance difficult to accomplish in this study. However, the major advantage of this approach is that it does away with the need for a spectrally characterized reflectance standard for the UV, a major issue (Hapke and Wells, 1981). A final issue is that rock surfaces, even roughened ones, are expected to be darker than powdered samples.

A.5. "Dollfus group" (1976–1980)

The UV spectral reflectance properties of a wide range of terrestrial and planetary materials were measured by Hua et al. (1976)

and Dollfus et al. (1980). Measurements of both macro (6 mm diameter spot size; Hua et al., 1976) and micro (1.5 mm diameter spot size; Dollfus et al., 1980) samples were made. For the macro samples, measurements were made across the range 200 to 700 nm for pulverized (<25 μm grain size) samples. Spectra were measured relative to freshly prepared MgO and $BaSO_4$. They noted that the reflectance of these materials falls rapidly below ~230 nm and that "weak values of albedo" around 250 nm are caused by some impurity absorptions (presumably in the reflectance standards). A xenon light source was used for illumination and passed through a monochromator. Samples and standards were both viewed with a phase angle of 5°. Spectral resolution varied from 2 nm below 230 nm to 1 nm in the blue visible region. Apparently, no attempt was made to correct for the decrease in reflectance of the standards below ~230 nm, which would result in anomalously high reflectance for the samples.

For the micro-scale measurements (Dollfus et al., 1980), broadband light from a Leitz Ultropak illuminator was passed through a prism monochromator that provided a spectral resolution between 4 and 12 nm. This light was directed onto the sample by an annular condenser and all light scattered within a 70° solid angle was collected by the objective and directed onto a photomultiplier. Measurements were made relative to Eastman White Reflectance Standard (compressed $BaSO_4$). Only selected samples were spectrally characterized with the microscope system.

The lunar samples (breccias, rock surfaces and saw dust) generally exhibited increasing reflectance from 200 to 400 nm. Many of the sample spectra showed broad and shallow absorption bands in the 300 to 400 nm range that were attributed to various charge transfers (Hua et al., 1976). The lunar and a few of the mineral sample spectra (e.g., anorthosite) exhibited increasing reflectance toward longer wavelengths with reflectance minima near 240 nm. This could potentially be attributable to the uncorrected decrease in reflectance of the standards below this wavelength value. The majority of the mineral spectra exhibited reflectance increasing toward longer wavelengths, and a flattening-out of the spectrum below ~230 nm. The use of an identical viewing system for both samples and standards obviates many of the potential errors in deriving absolute albedos for the samples. However, the lack of a correction for the expected decrease in absolute reflectance of the MgO and $BaSO_4$ standards below ~230 nm may cause the apparent reflectance of the samples below ~230 nm to be anomalously high.

A.6. Nitsan and Shankland (1976)

Nitsan and Shankland (1976) measured unpolarized reflectance spectra of a number of silicates across the 4–14 eV range, which includes the 200 to 400 nm range, using a McPherson model 225 1-meter normal incidence monochromator. Incident light was measured directly by the detector as the reference and specularly reflected off the sample. The detector consisted of a sodium salicylate-coated light pipe and photomultiplier tube. Spectral resolution was ~1–2 nm. They identified the major uncertainties in their measurements as being due to non-uniform coating of the fluorescent material on the detector and scattered light. They ascribed spurious internal and back-surface reflections to the increase in apparent reflection as wavelength increased from ~300 to 400 nm. Given the geometry of their experimental setup, absolute reflectance is not readily derivable. In addition the use of polished solid samples led to apparently anomalous reflectance increases above ~300 nm and the relationship of solid to powdered sample reflectance is not straightforward.

A.7. Strens and Wood (1979)

Strens and Wood (1979) measured 200–2500 nm diffuse reflectance spectra of a number of Fe, Ti, and Fe–Ti oxides and hydroxides using a Unicam SP700C spectrophotometer fitted with an SP735 diffuse reflectance accessory. Spectra were measured relative to freshly prepared MgO smoke, produced from burning Mg ribbon. They found that many of their samples exhibited absorption bands in the 200–400 nm interval, most of which were assigned to various metal–O charge transfers.

A.8. Hofmeister and Rossman (1984)

Hofmeister and Rossman (1984) measured absorbance spectra (320–2800 nm) on oriented polished slabs of plagioclase feldspars using a Cary 17I spectrometer. Few other details of the instrument set-up were provided. The plagioclase spectra show absorbance decreasing from 320 to 400 nm, with a number of superimposed absorption bands in the 380–450 nm interval. The relevance of this work to the present study is uncertain due to the general lack of experimental details and the use of slabs instead of powders; other investigators have shown that overall spectral slopes can differ between spectra of powders and slabs (e.g., Hapke et al., 1978).

A.9. Shkuratov et al. (1985)

Shkuratov et al. (1985) measured reflectance spectra of <200 μm size powders of two eucrites (Chernovy Kut and Stannern) over the range 260–1050 nm using a Hitachi EPS-3T spectrometer. No other details of the spectral measurements were provided. The two spectra show reflectance decreasing below 400 nm, with Chernovy Kut exhibiting minimum reflectance near 300 nm and Stannern showed reflectance continuing to decrease to at least 260 nm. The lack of experimental details makes critical evaluation of the validity of their results impossible.

A.10. Wagner et al. (1987)

Wagner et al. (1987) measured 92–1800 nm reflectance spectra of a number of planetary materials (<74 μm grain size). Spectra from 200 to 1800 nm were measured with a Cary 14 spectrophotometer with a bidirectional reflectance attachment operating at $i = 30°$ and $e = 30°$. Sample reflectance was measured relative to a calibrated $BaSO_4$ standard. Both standard and sample were measured with the same viewing geometry and apparatus (Hapke and Wells, 1981). The standard consisted of multiple layers of Eastman Kodak White Reflectance Paint with a total thickness of 3 mm deposited on a glass slide. The absolute reflectance of the standard was found to agree well with previously determined values between 250 and 1700 nm (Grum and Luckey, 1968). The absolute reflectance in the 200 to 250 nm region was adjusted from the published values by measuring the spectral absorption coefficient of fused silica. The difference in reflectance of the $BaSO_4$ in the 200 to 225 nm region between Grum and Luckey (1968) and Hapke and Wells (1981) is on the order of 15% absolute at 220 nm, and is likely much larger at 200 nm.

Appendix B. Experimental details of previous laboratory UV investigations

B.1. Detectors

A number of the previous studies made use of a fluorescent sodium salicylate coating on one end of a light pipe coupled to a photomultiplier tube. Sodium salicylate is a very efficient converter of UV photons with energies between 60 and 360 nm (Allison et

al., 1964). Incident photons are converted to visible photons with energies centered around 443 nm, and the fluorescent quantum yield is widely assumed to be independent of wavelength over the 60–360 nm range, although this may not be totally accurate (Allison et al., 1964). Sodium salicylate is very stable and the only potential issue which could affect the measurements would be non-uniform coating thickness, however this is likely not a significant consideration for the vast majority of the studies discussed in this paper.

B.2. Monochromatic light source and broadband detector

Extraterrestrial targets such as the Moon are irradiated by broad-band (polychromatic) radiation, which may result in fluorescence of target minerals (e.g., Flynn et al., 1998). Spectral measurements acquired in the laboratory utilizing monochromatic illumination and broad-band detectors would thus not necessarily provide spectral data directly comparable to observational data if target fluorescence effects are present. As an example, consider a mineral that has similar fluorescence response as halon; i.e., that it absorbs some portion of light below ∼250 nm and re-emits some of this energy at longer wavelengths (∼300–350 nm). If spectral measurements are made at 325 nm using a monochromatic light source and broadband detector, the spectral reflectance of the sample will not include the additional fluorescence-induced light that would otherwise be detected from a planetary surface. Thus, the laboratory spectrum would appear darker in the wavelength interval of induced fluorescence than it would on a surface irradiated by fluorescence-inducing broad-band radiation. Consequently, if we wish to properly simulate how solar radiation may interact with a surface, and hence to confidently utilize laboratory spectral data for interpretation of observational data, broad-band sample illumination should be used.

B.3. Suitability of reflectance standards

A major issue facing attempts to accurately measure absolute spectral reflectance properties of materials in the UV is the availability of reliable or well-characterized reflectance standards. Previous measurements of the UV spectral reflectance properties of geological materials have generally been undertaken in one of two ways: (1) through the use of a reflectance standard, where both samples and standards are measured with identical viewing geometries and instrumentation (e.g., Strens and Wood, 1979; Hapke and Wells, 1981; Wagner et al., 1987), and (2) directing the incident light directly at the detector for the standard measurements, while the samples are viewed generally in bidirectional mode (e.g., Carver et al., 1975; Nitsan and Shankland, 1976; Cohen et al., 1978; Hapke et al., 1978; Wagner et al., 1979, 1987; Wagner, 1980).

In the case where reflectance standards are viewed in the same way as the samples, the major uncertainty lies in the absolute reflectance values of the standards that are employed. Commonly used standards include MgO smoke, $BaSO_4$, and halon (polytetrafluoroethylene powder); the relative benefits and disadvantages of each are described below.

B.3.1. MgO smoke

MgO has perhaps the longest legacy of use as a reflectance standard. Freshly prepared MgO, produced by combusting Mg, can be used as a reflectance standard. The Commission Internationale de L'Eclairage (1979) provides a comprehensive summary of the suitability of MgO as a reflectance standard. They note that the reflectance of freshly smoked MgO can be affected by factors such as the co-production of magnesium nitride due to combustion in air, decrease in reflectance due to aging (possibly from the production of a carbonate coating), its hygroscopic nature, and difficulties in reproducibility of a coating. Pressed MgO is generally more stable than smoked MgO. Grum and Luckey (1968) found that the absolute reflectance of smoked MgO was 86.5% (fresh) or 67.2% (aged 2 months) at 225 nm, with reflectance increasing gradually toward longer wavelengths, to a maximum of ∼98% (fresh) between 400 and 800 nm, and decreasing again toward longer wavelengths.

B.3.2. $BaSO_4$

$BaSO_4$ is another commonly used reflectance standard. It is more stable than MgO, shows long-term (decades) stability, is insensitive to high levels of irradiation, has higher reflectance in the UV, and exhibits little sensitivity to humidity and UV irradiation. Prolonged irradiance with light of wavelengths $\lesssim$270 nm may cause a few percent decrease in absolute reflectance, and may lead to optical absorption and exoelectron emission around 320 nm due to the production of electron traps, but this effect is reversible (Commission Internationale de L'Eclairage, 1979). Fluorescence in $BaSO_4$ is less (3%) than in halon (17%) at 340 nm (Saunders and Ott, 1976). Absolute reflectance measurements of $BaSO_4$ indicate that its reflectance is between 90.5% ($BaSO_4$ paint) and 92.5% (pressed powder) at 225 nm, increasing gradually to >99% at 375 nm (pressed powder) or 450 nm ($BaSO_4$ paint) (Grum and Luckey, 1968). Hapke and Wells (1981) used $BaSO_4$ as a reflectance standard for some UV spectral reflectance measurements. They determined, through a different procedure than ASTM (1966) that the absolute reflectance of their Eastman Kodak White Reference Paint was substantially lower than the values determined by Grum and Luckey (1968) in the UV. At 225 nm, their determined absolute reflectance was ∼80% versus 90.5% measured by Grum and Luckey (1968).

B.3.3. Halon powder

Pressed halon (polytetrafluoroethylene) powder has become an increasingly popular reflectance standard (e.g., RELAB, 2006). Its absolute reflectance exceeds 95% between 220 and 2500 nm and it is highly Lambertian (Weidner and Hsia, 1981). Weidner and Hsia (1981) noted that halon shows little evidence of fluorescence when measured both with monochromatic and polychromatic radiation. They noted that there appears to be a slight amount of fluorescence with excitation at wavelengths less than 290 nm and emission in the wavelength range of 310 to 350 nm and that this fluorescence could become significant if ultraviolet radiation below 300 nm is involved.

Earlier work by Saunders and Ott (1976) compared the spectral reflectance properties of halon to $BaSO_4$. They attributed the large discrepancies in reflectance (up to 17%) over the 280 to 350 nm range to fluorescence by the halon induced by short wavelength irradiation. They cautioned that spectral measurements made using radiation sources with a UV output that is significant compared to output at longer wavelengths could lead to anomalously high apparent reflectance due to the fluorescence induced by the short wavelength radiation.

B.3.4. Comparison of standards

The absolute reflectance properties of halon, $BaSO_4$ (paint or pressed powder), and fresh MgO are all very similar over the 250–700 nm range (Grum and Saltzman, 1976). However, as noted, these similarities and the suitability of a particular standard seem to be highly dependent on the experimental conditions, such as low UV to visible flux, and use of a broadband versus monochromatic light source. As discussed above, halon appears to absorb some portion of low wavelength (<250 nm) ultraviolet radiation, some or all of which is re-emitted at longer wavelengths (Saunders and Ott, 1976; Commission Internationale de L'Eclairage, 1979). The degradation and fluorescence effects have been little noted in the

past because the vast majority of studies have been conducted at wavelengths >250 nm or with monochromatic light sources and/or detectors. The fluorescence effects become noticeable when short wavelength irradiation (<250 nm) is a significant fraction of the incident radiation.

B.4. Standardless measurements

The problems associated with the commonly used reflectance standards can be overcome in two ways: by comparing spectral reflectance of a sample to a standard-free measure of incident radiation; i.e., by directing the incident beam alternatively directly onto the detector or the sample (e.g., Carver et al., 1975; Nitsan and Shankland, 1976; Cohen et al., 1978; Hapke et al., 1978; Wagner et al., 1979, 1980; Wagner, 1980), or through independent determinations of the absolute reflectance of the standard (e.g., Hapke and Wells, 1981; Wagner et al., 1987). The major shortcoming of the first approach is that if all of the light reflected by the sample is not collected, absolute reflectance cannot be determined. However, this approach has the advantage of providing the most robust measure of relative reflectance, as no standard, which may have unknown or undesirable spectral reflectance properties, is used. This procedure remains robust if the light reflected off the sample is measured directly by the detector (as is the case for the direct incident radiation used as the "standard"), and path lengths and optical trains are the same for both standard and sample (i.e., no intervening optical elements that would introduce their own spectral modifications).

In the second approach, absolute reflectance is potentially derivable, and the major issue is identifying a reflectance standard whose absolute spectral reflectance properties are well characterized. As discussed above, the suitability of a reflectance standard may be a function of the spectral distribution of the incident radiation. It appears that as the intensity of UV (particularly <250 nm) to longer wavelength radiation increases, the greater the deviations from absolute reflectance that may be introduced. This is compounded by the paucity of absolute reflectance data below ~250 nm for potential diffuse reflectance standards.

References

Adams, J.B., 1974. Visible and near-infrared diffuse reflectance spectra of pyroxenes as applied to remote sensing of solid objects in the Solar System. J. Geophys. Res. 79, 4829–4836.

Adams, J.B., Goullaud, L.H., 1978. Plagioclase feldspars: Visible and near-infrared diffuse reflectance spectra as applied to remote sensing. Proc. Lunar Sci. Conf. 9, 2901–2909.

Adams, J.B., McCord, T.B., 1973. Vitrification darkening in the lunar highlands and identification of Descartes material at the Apollo 16 site. Proc. Lunar Sci. Conf. 4, 163–177.

Allison, R., Burns, J., Tuzzolino, A.J., 1964. Absolute fluorescent quantum efficiency of sodium salicylate. J. Opt. Soc. Am. 54, 747–751.

Antipova-Karataeva, I.I., Stacheev, Yu.I., Tarasov, L.S., 1973. Absorption spectra of lunar sections from different lunar areas. Space Res. XIII, 997–1000.

ASTM, 1966. Standard Method for Absolute Calibration of Reflectance Standards. Book of ASTM Standards E306–66, American Society for Testing and Materials, West Conshohocken, PA, pp. 986–989.

Atkinson, S.S., 1990. Geochemical and isotopic study of the Roza member feeder system, Columbia River basalt group. M.Sc. thesis, Univ. Alberta, Edmonton, AB, 112 pp.

Badro, J., Rueff, J.-P., Vankó, G., Monaco, G., Fiquet, G., Guyot, F., 2004. Electronic transitions in perovskite: Possible nonconvecting layers in the lower mantle. Science 305, 383–386.

Bandfield, J.L., 2002. Global mineral distributions on Mars. J. Geophys. Res. 107, doi:10.1029/2001JE001510.

Banin, A., Han, F.X., Kan, I., Cicelsky, A., 1997. Acidic volatiles and the Mars soil. J. Geophys. Res. 102, 13341–13356.

Barth, C.A., Hord, C.W., 1971. Mariner ultraviolet spectrometer: Topography and polar cap. Science 173, 197–201.

Bell, P.M., Mao, H.K., 1973. Optical and chemical analysis of iron in Luna 20 plagioclase. Geochim. Cosmochim. Acta 37, 755–759.

Bell III, J.F., 1992. Charge-coupled device imaging spectroscopy of Mars. 2. Results and implications for martian ferric mineralogy. Icarus 100, 575–597.

Bell III, J.F., Ansty, T., 2007. High spectral resolution UV to near-IR observations of Mars during 1999, 2001, and 2003 using HST/STIS. Icarus 191, 581–602.

Bell III, J.F., Crisp, D., 1993. Groundbased imaging spectroscopy of Mars in the near-infrared: Preliminary results. Icarus 104, 2–19.

Bell III, J.F., Pollack, J.B., Geballe, T.R., Cruikshank, D.P., Freedman, R., 1994. Spectroscopy of Mars from 2.04 to 2.44 μm during the 1993 opposition: Absolute calibration and atmospheric vs. mineralogic origin of narrow absorption features. Icarus 111, 106–123.

Bell III, J.F., Wolff, M.J., James, P.B., Clancy, R.T., Lee, S.W., Martin, L.J., 1997. Mars surface mineralogy from Hubble Space Telescope imaging during 1994–1995: Observations, calibration, and initial results. J. Geophys. Res. 102, 9109–9123.

Bertaux, J.-L., Korablev, O., Perrier, S., Quémerais, E., Montmessin, F., Leblanc, F., Lebonnois, S., Rannou, P., Lefèvre, F., Forget, F., Fedorova, A., Dimarellis, E., Reberac, A., Fonteyn, D., Chaufray, J.Y., Guibert, S., 2006. SPICAM on Mars Express: Observing modes and overview of UV spectrometer data and scientific results. J. Geophys. Res. 111, doi:10.1029/2006JE002690. E10S90.

Bevan, H., Dawes, S.V., Ford, R.A., 1958. The electronic spectra of titanium dioxide. Spectrochim. Acta 13, 43–49.

Blaney, D.B., McCord, T.B., 1989. Indications of sulfate minerals in the martian soil from Earth-based spectroscopy. J. Geophys. Res. 94, 10159–10166.

Blazey, K.W., 1977. Optical absorption of MgO:Fe. J. Phys. Chem. Solids 38, 671–675.

Blewett, D.T., Lucey, P.G., Hawke, B.R., Joliff, B.L., 1997. Clementine images of the lunar sample-return stations: Refinement of FeO and TiO_2 mapping techniques. J. Geophys. Res. 102, 16319–16325.

Blewett, D.T., Hawke, B.R., Lucey, P.G., 2002. Lunar pure anorthosite as a spectral analog for Mercury. Meteorit. Planet. Sci. 37, 1245–1254.

Blewett, D.T., Hawke, B.R., Lucey, P.G., Robinson, M.S., 2007. A Mariner 10 color study of mercurian craters. J. Geophys. Res. 112, doi:10.1029/2006JE002713. E02005.

Burns, R.G., 1970. Crystal field spectra and evidence of cation ordering in olivine minerals. Am. Mineral. 55, 1608–1632.

Burns, R.G., 1981. Intervalence transitions in mixed-valence minerals of iron and titanium. Annu. Rev. Earth Planet. Sci. 9, 345–383.

Burns, R.G., 1987. Ferric sulfates on Mars. J. Geophys. Res. 92, E570–E574.

Burns, R.G., 1993a. Rates and mechanisms of chemical weathering of ferromagnesian silicate minerals on Mars. Geochim. Cosmochim. Acta 57, 4555–4574.

Burns, R.G., 1993b. Mineralogical Applications of Crystal Field Theory, second ed. Cambridge Univ. Press, Cambridge, UK, 551 pp.

Burns, R.G., Parkin, K.M., Loeffler, B.M., Leung, I.S., Abu-Eid, R.M., 1976. Further characterization of spectral features attributable to titanium on the Moon. Proc. Lunar Sci. Conf. 7, 2561–2578.

Butterworth, P.S., Meadows, A.J., 1985. Ultraviolet reflectance properties of asteroids. Icarus 62, 305–318.

Calvin, W.M., Clark, R.N., Brown, R.H., Spencer, J.R., 1995. Spectra of the icy Galilean satellites from 0.2 to 5 μm: A compilation, new observations, and a recent summary. J. Geophys. Res. 100, 19041–19048.

Carlson, R.W., Anderson, M.S., Johnson, R.E., Smythe, D.W., Hendrix, A.R., Barth, C.A., Soderblom, L.A., Hansen, G.B., McCord, T.B., Dalton, J.B., Clark, R.N., Shirley, J.H., Ocampo, A.C., Matson, D.L., 1999. Hydrogen peroxide on the surface of Europa. Science 283, 2062–2064.

Carver, J.H., Horton, B.H., O'Brien, R.S., O'Connor, G.G., 1974. The ultraviolet reflectivity of the Moon. Moon 9, 295–303.

Carver, J.H., Horton, B.H., McCoy, D.G., O'Brien, R.S., Sandercock, E.R., 1975. Comparison of lunar ultraviolet reflectivity with that of terrestrial rock samples. Moon 12, 91–100.

Charette, M.P., McCord, T.B., Pieters, C., Adams, J.B., 1974. Application of remote sensing spectral reflectance measurements to lunar geology classification and determination of titanium content of lunar soils. J. Geophys. Res. 79, 1605–1613.

Chin, G., Brylow, S., Foote, M., Garvin, J., Kasper, J., Keller, J., Litvak, M., Mitrofanov, I., Paige, D., Raney, K., Robinson, M., Sanin, A., Smith, D., Spence, H., Spudis, P., Stern, S.A., Zuber, M., 2007. Lunar Reconnaissance Orbiter overview: The instrument suite and mission. Space Sci. Rev. 129, 391–419.

Christensen, P.R., Ruff, S.W., 2004. Formation of the hematite-bearing unit in Meridiani Planum: Evidence for deposition in standing water. J. Geophys. Res. 109, doi:10.1029/2003JE002233. E08003.

Christensen, P.R., Morris, R.V., Lane, M.D., Bandfield, J.L., Malin, M.C., 2001. Global mapping of martian hematite mineral deposits: Remnants of water-driven processes on early Mars. J. Geophys. Res. 106, 23873–23885.

Clark, R.N., Swayze, G.A., Singer, R.B., Pollack, J.B., 1990. High-resolution reflectance spectra of Mars in the 2.3-μm region: Evidence for the mineral scapolite. J. Geophys. Res. 95, 14463–14480.

Cloutis, E.A., 2002. Pyroxene reflectance spectra: Minor absorption bands and effects of elemental substitutions. J. Geophys. Res. 107, doi:10.1029/2001JE001590.

Cloutis, E.A., Bell III, J.F., 2004. Mafic silicate mapping on Mars: Effects of palagonitic material, multiple mafic silicates, and spectral resolution. Icarus 172, 233–254.

Cloutis, E.A., Gaffey, M.J., 1991. Pyroxene spectroscopy revisited: Spectral–compositional correlations and relationship to geothermometry. J. Geophys. Res. 96, 22809–22826.

Cloutis, E.A., Gaffey, M.J., Smith, D.G.W., Lambert, R.St.J., 1990. Reflectance spectra of glass-bearing mafic silicate mixtures and spectral deconvolution procedures. Icarus 86, 383–401.

Cohen, A.J., Wagner, J.K., Hapke, B.W., Partlow, W.D., 1978. Vacuum ultraviolet spectra of carbonaceous chondrites. Meteoritics 13, 420–427.

Commission Internationale de L'Eclairage, 1979. A review of publications on properties and reflection values of material reflection standards. Publication CIE No. 46, Paris, France.

Conel, J.E., Nash, D.B., 1970. Spectral reflectance and albedo of Apollo 11 lunar samples: Effects of irradiation and vitrification and comparison with telescopic observations. In: Levinson, A.A. (Ed.), Proc. Apollo 11 Lunar Sci. Pergamon Press, New York, pp. 2013–2023.

Cooper, B., Potter, A., Killen, R., Morgan, T., 2001. Midinfrared spectra of Mercury. J. Geophys. Res. 106, 32803–32814.

Deer, W.A., Howie, R.A., Zussman, J., 1997. Rock Forming Minerals, vol. 1A. Orthosilicates, second ed. The Geological Society, London, UK, 919 pp.

Deer, W.A., Howie, R.A., Zussman, J., 2001. Rock Forming Minerals, vol. 4A. Framework Silicates: Feldspars, second ed. The Geological Society, London, UK, 972 pp.

Dollfus, A., Cailleux, A., Cervelle, B., Hua, C.T., Mandeville, J.-C., 1980. Reflectance spectroscopy extended to u.v. for terrestrial, lunar and meteoritic samples. Geochim. Cosmochim. Acta 44, 1293–1310.

Elphic, R.C., Lawrence, D.J., Feldman, W.C., Barraclough, B.L., Gasnault, O.M., Maurice, S., Lucey, P.G., Blewett, D.T., Binder, A.B., 2002. Lunar Prospector neutron spectrometer constraints on TiO_2. J. Geophys. Res. 107, doi:10.1029/2000JE001460.

Flynn, B.C., Vallerga, J.V., Gladstone, G.R., Edelstein, J., 1998. Lunar reflectivity from Extreme Ultraviolet Explorer imaging and spectroscopy of the full Moon. Geophys. Res. Lett. 25, 3253–3256.

Garvin, J.B., Robinson, M.S., Hapke, B., Bell III, J.F., Skillman, D., Ulmer, M., Pieters, C., 2006. UV imaging of the Moon from the Hubble Space Telescope. Lunar Planet. Sci. 37. Abstract 2100 [CD ROM].

Gendrin, A., Mangold, N., Bibring, J.-P., Langevin, Y., Gondet, B., Poulet, F., Bonello, G., Quantin, C., Mustard, J., Arvidson, R.E., LeMouélic, S., 2005. Sulfates in martian layered terrains: The OMEGA/Mars Express view. Science 307, 1587–1591.

Gillis, J.J., Jolliff, B.L., Elphic, R.C., 2003. A revised algorithm for calculating TiO_2 from Clementine UVVIS data: A synthesis of rock, soil, and remotely sensed TiO_2 concentrations. J. Geophys. Res. 108, doi:10.1029/2001JE001515.

Gold, R.E., Solomon, S.C., McNutt Jr., R.L., Santo, A.G., Abshire, J.B., Acuña, M.H., Afzal, R.S., Anderson, B.J., Andrews, G.B., Bedini, P.D., Cain, J., Cheng, A.F., Evans, L.G., Feldman, W.C., Follas, R.B., Gloeckler, G., Goldsten, J.O., Hawkins III, S.E., Izenberg, N.R., Jaskulek, S.E., Ketchum, E.A., Lankton, M.R., Lohr, D.A., Mauk, B.H., McClintock, W.E., Murchie, S.L., Schlemm II, C.E., Smith, D.E., Starr, R.D., Zurbuchen, T.H., 2001. The MESSENGER mission to Mercury: Scientific payload. Planet. Space Sci. 49, 1467–1479.

Gooding, J.L., 1978. Chemical weathering on Mars. Icarus 33, 483–513.

Greenman, N.N., Burkig, V.W., Young, J.F., 1967. Ultraviolet reflectance measurements of possible lunar silicates. J. Geophys. Res. 72, 1355–1359.

Grum, F., Luckey, G.W., 1968. Optical sphere paint and a working standard of reflectance. Appl. Opt. 7, 2289–2294.

Grum, F., Saltzman, M., 1976. New white standard of reflectance. Intl. Comm. Illum. 18, 91–98.

Hapke, B., 2001. Space weathering from Mercury to the asteroid belt. J. Geophys. Res. 106, 10039–10073.

Hapke, B., Wells, E., 1981. Bidirectional reflectance spectroscopy. 2. Experiments and observations. J. Geophys. Res. 86, 3055–3060.

Hapke, B.W., Partlow, W.D., Wagner, J.K., Cohen, A.J., 1978. Reflectance measurements of lunar materials in the vacuum ultraviolet. Proc. Lunar Sci. Conf. 9, 2935–2947.

Hawthorne, F.C., Krivovichev, S.V., Burns, P.C., 2000. The crystal chemistry of sulfate minerals. In: Alpers, C.N., Jambor, J.L., Nordstrom, D.K. (Eds.), Sulfate Minerals: Crystallography, Geochemistry, and Environmental Significance. In: Reviews in Mineralogy, vol. 40. Mineralogical Society of America, Washington, DC, pp. 1–112.

Heiken, G.H., Vaniman, D.T., French, B.M., 1991. Lunar Sourcebook: A User's Guide to the Moon. Cambridge University Press, Cambridge, UK, 736 pp.

Hendrix, A.R., Vilas, F., 2006. The effects of space weathering at UV wavelengths: S-class asteroids. Astron. J. 132, 1396–1404.

Hendrix, A.R., Barth, C.A., Hord, C.W., Lane, A.L., 1998. Europa: Disk-resolved ultraviolet measurements using the Galileo ultraviolet spectrometer. Icarus 135, 79–94.

Hendrix, A.R., Simmons, K.E., Mankoff, K.D., 2003. Characterizing the oxidizing properties of Mars' polar regions. In: Sixth Intl. Conf. on Mars. Abstract 3254 [CD ROM].

Hofmeister, A.M., 2005. Dependence of diffusive radiative transfer on grain-size, temperature, and Fe-content: Implications for mantle processes. J. Geodyn. 40, 51–72.

Hofmeister, A.M., Rossman, G.R., 1984. Determination of Fe^{3+} and Fe^{2+} concentrations in feldspar by optical absorption and EPR spectroscopy. Phys. Chem. Miner. 11, 213–224.

Hord, C.W., Barth, C.A., Pearce, J.B., 1970. Ultraviolet spectroscopy experiment for Mariner Mars 1971. Icarus 12, 63–71.

Hua, C.T., Dollfus, A., Mandeville, J.-C., 1976. Ultraviolet diffuse reflectance spectroscopy for lunar, meteoritic, and terrestrial samples. Proc. Lunar Sci. Conf. 7, 2605–2622.

Hunt, G.R., Salisbury, J.W., 1970. Visible and near-infrared spectra of minerals and rocks. I. Silicates. Mod. Geol. 1, 283–300.

Keppler, H., McCammon, C.A., Rubie, D.C., 1994. Crystal-field and charge-transfer spectra of $(Mg,Fe)SiO_3$ perovskite. Am. Mineral. 79, 1215–1218.

Klingelhöfer, G., Morris, R.V., Berhradt, B., Schröder, C., Rodionov, D., de Souza, P.A.J., Yen, A.S., Gellert, R., Evlanov, E.N., Zubkov, B., Foh, J., Bonnes, U., Kankeleit, E., Gütlich, P., Ming, D.W., Renz, F., Wdowiak, T.J., Squyres, S.W., Arvidson, R.E., 2004. Jarosite and hematite at Meridiani Planum from Opportunity's Mössbauer spectrometer. Science 306, 1740–1745.

Langevin, Y., Poulet, F., Bibring, J.-P., Gondet, B., 2005. Sulfates in the north polar region of Mars detected by OMEGA/Mars Express. Science 307, 1584–1586.

Lebedinsky, A.I., Krasnopolsky, V.A., Krysko, A.A., 1967a. The spectrophotometric measurements of the Moon in the 1900–2750 A range from the Zond 3 automatic space probe. In: Dollfus, A. (Ed.), Moon and Planets. N. Holland Publ. Co., Amsterdam, pp. 59–64.

Lebedinsky, A.I., Aleshin, G.M., Iozenas, V.A., Krasnopolsky, V.A., Selivanov, A.S., Zasetsky, V.V., 1967b. The lunar ultraviolet spectrum in the range of 2850–3550 A according to data obtained from the Zond 3 automatic space probe. In: Dollfus, A. (Ed.), Moon and Planets. N. Holland Publ. Co., Amsterdam, pp. 65–70.

Lebedinsky, A.I., Krasnopolsky, V.A., Aganina, M.U., 1968. The spectral albedo of the Moon's surface in the mid-ultraviolet according to data from the Zond-3 space probe. In: Dollfus, A. (Ed.), Moon and Planets II. N. Holland Publ. Co., Amsterdam, pp. 47–54.

Loeffler, B.M., Burns, R.G., Tossell, J.A., Vaughan, D.G., Johnson, K.H., 1974. Charge transfer in lunar materials: Interpretation of ultraviolet–visible spectral properties of the Moon. Geochim. Cosmochim. Acta 3 (Suppl. 5), 3007–3016.

Lucey, P.G., Blewett, D.T., Hawke, B.R., 1998. Mapping the FeO and TiO_2 content of the lunar surface with multispectral imagery. J. Geophys. Res. 103, 3679–3699.

Lucey, P.G., Blewett, D.T., Jolliff, B.L., 2000. Lunar iron and titanium abundance algorithms based on final processing of Clementine ultraviolet–visible images. J. Geophys. Res. 105, 20297–20305.

Lucke, R.L., Henry, R.C., Fastie, W.G., 1973. Far ultraviolet reflectivity of lunar dust samples: Apollo 11, 12, and 14. Astron. J. 78, 263–267.

Lucke, R.L., Henry, R.C., Fastie, G.W., 1974. Far-ultraviolet lunar mapping from Apollo 17. Proc. Lunar Sci. Conf. 5, 469–471.

Lucke, R.L., Henry, R.C., Fastie, W.G., 1976. Far-ultraviolet albedo of the Moon. Astron. J. 81, 1162–1169.

Lumpkin, G.R., Ribbe, P.H., 1983. Composition, order–disorder and lattice parameters of olivines: Relationships in silicate, germinate, beryllate, phosphate and borate olivines. Am. Mineral. 68, 164–176.

Malin M.C., 2006. Initial observations by the MRO Mars Color Imager and Context Camera. In: Am. Geophys. Union Fall Meeting 2006. Abstract P33A-03.

McClure, D.S., 1962. Optical spectra of transition-metal ions in corundum. J. Chem. Phys. 36, 2757–2779.

Melendrez, D.E., Johnson, J.R., Larson, S.M., Singer, R.B., 1994. Remote sensing of potential lunar resources. 2. High spatial resolution mapping of spectral reflectance ratios and implications for nearside mare TiO_2 content. J. Geophys. Res. 99, 5601–5619.

Mertzman, S.A., 2000. K–Ar results from the southern Oregon–northern California Cascade Range. Oregon Geol. 62, 99–122.

Morris, R.V., 1980. Origins and size distributions of metallic iron particles in the lunar regolith. Proc. Lunar Sci. Conf. 11, 1697–1712.

Morris, R.V., Agresti, D.G., Lauer Jr., H.V., Newcomb, J.A., Shelfer, T.D., Murali, A.V., 1989. Evidence for pigmentary hematite on Mars based on optical, magnetic, and Mössbauer studies of superparamagnetic (nanocrystalline) hematite. J. Geophys. Res. 94, 2760–2778.

Morris, R.V., Golden, D.C., Bell III, J.F., Lauer Jr., H.V., Adams, J.B., 1993. Pigmenting agents in martian soils: Inferences from spectral, Mossbauer, and magnetic properties of nanophase and other iron oxides in Hawaiian palagonitic soil PN-9. Geochim. Cosmochim. Acta 57, 4597–4609.

Morris, R.V., Golden, D.C., Bell III, J.F., Shelfer, T.D., Scheinost, A.C., Hinman, N.W., Furniss, G., Mertzman, S.A., Bishop, J.L., Ming, D.W., Allen, C.C., Britt, D.T., 2000. Mineralogy, composition, and alteration of Mars Pathfinder rocks and soils: Evidence from multispectral, elemental, and magnetic data on terrestrial analogue, SNC meteorite, and Pathfinder samples. J. Geophys. Res. 105, 1757–1817.

Morris, R.V., Golden, D.C., Ming, D.W., Shelfer, T.D., Jørgensen, Bell III, J.F., Graff, T.G., Mertzman, S.A., 2001. Phyllosilicate-poor palagonitic dust from Mauna Kea Volcano (Hawaii): A mineralogical analogue for magnetic martian dust? J. Geophys. Res. 106, 5057–5083.

Mulcahy, C.K., Taylor, L.A., Goodrich, C.A., 2004. A comparison of textural and chemical features of spinel within lunar mare basalts. Lunar Planet. Sci. 35. Abstract 1331 [CD ROM].

Murchie, S., Mustard, J., Bishop, J., Head, J., Pieters, C., Erard, S., 1993. Spatial variations in the spectral properties of bright regions on Mars. Icarus 105, 454–468.

Nash, D.B., Conel, J.E., 1971. Luminescence and reflectance of Apollo 12 samples. Proc. Lunar Sci. Conf. 2, 2235–2244.

Nitsan, U., Shankland, T.J., 1976. Optical properties and electronic structure of mantle silicates. Geophys. J. R. Astron. Soc. 45, 59–87.

Noble, S.K., Pieters, C.M., Taylor, L.A., Morris, R.V., Allen, C.C., McKay, D.S., Keller, L.P., 2001. The optical properties of the finest fraction of lunar soil: Implications for space weathering. Meteorit. Planet. Sci. 36, 31–42.

Noble, S.K., Pieters, C.M., Keller, L.P., 2003. The optical properties of nanophase iron: Investigation of a space weathering analog. Lunar Planet. Sci. 34. Abstract 1172 [CD ROM].

Noble, S.K., Pieters, C.M., Keller, L.P., 2007. An experimental approach to understanding the optical effects of space weathering. Icarus 192, 629–642.

Noll, K.S., Weaver, H.A., Gonnella, A.M., 1995. The albedo spectrum of Europa from 2200 Å to 3300 Å. J. Geophys. Res. 100, 19057–19059.

O'Connor, J.T., 1968. Mineral stability at the martian surface. J. Geophys. Res. 73, 5301–5311.

Pang, K., Ajello, J.M., 1977. Complex refractive index of martian dust: Wavelength dependence and composition. Icarus 30, 63–74.

Pang, K.D., Chun, S.F.S., Ajello, J.M., Nansheng, Z., Minji, L., 1982. Organic and inorganic interpretations of the martian UV-IR reflectance spectrum. Nature 295, 43–46.

Papike, J.J., Hodges, F.N., Bence, A.E., Cameron, M., Rhodes, J.M., 1976. Mare basalts: Crystal chemistry, mineralogy, and petrology. Rev. Geophys. Space Phys. 14, 475–540.

Papike, J., Taylor, L., Simon, S., 1991. Lunar minerals. In: Heiken, G.H., Vaniman, D.T., French, B.M. (Eds.), Lunar Sourcebook: A User's Guide to the Moon. Cambridge University Press, New York, pp. 121–181.

Pollack, J.B., Roush, T.L., Witteborn, F., Bregman, J., Wooden, D., Stoker, C., Toon, O.B., Rank, D., Dalton, B., Freedman, R., 1990. Thermal emission spectra of Mars (5.4–10.5 μm): Evidence for sulfates, carbonates, and hydrates. J. Geophys. Res. 95, 14595–14627.

Poulet, F., Bibring, J.-P., Mustard, J.F., Gendrin, A., Mangold, N., Langevin, Y., Arvidson, R.E., Gondet, B., Gomez, C., and Omega Team, 2005. Phyllosilicates on Mars and implications for early martian climate. Nature 438, 623–627.

RELAB, 2006. Reflectance Experiment Laboratory User's Manual. Dept. of Geological Sci., Brown Univ., Providence, RI.

Riner, M.A., Robinson, M.S., Tangeman, J.A., Elphic, R.C., 2005. Is ilmenite always the dominant carrier of titanium in lunar mare basalts? Lunar Planet. Sci. 36. Abstract 1943 [CD ROM].

Robinson, M.S., Lucey, P.G., 1997. Recalibrated Mariner 10 color mosaics: Implications for mercurian volcanism. Science 275, 197–200.

Robinson, M.S., Taylor, G.J., 2001. Ferrous oxide in Mercury's crust and mantle. Meteorit. Planet. Sci. 36, 841–847.

Robinson, M.S., Garvin, J.B., Hapke, B., Bell III, J.F., Ulmer, M., Skillman, D., Pieters, C.M., 2006. HST UV–visible observations of the Apollo 17 landing area. Lunar Planet. Sci. 37. Abstract 2282 [CD ROM].

Robinson, M.S., Hapke, B.W., Garvin, J.B., Skillman, D., Bell III, J.F., Ulmer, M.P., Pieters, C.M., 2007. High resolution mapping of TiO_2 abundances on the Moon using the Hubble Space Telescope. Geophys. Res. Lett. 34, doi:10.1029/2007GL029754. L13203.

Saunders, R.D., Ott, W.R., 1976. Spectral irradiance measurements: Effect of UV-produced fluorescence in integrating spheres. Appl. Opt. 15, 827–828.

Shankland, T.J., Nitsan, U., Duba, A.G., 1979. Optical absorption and radiative heat transport in olivine at high temperature. J. Geophys. Res. 84, 1603–1610.

Sherman, D.M., 1983. The effect of local magnetic interactions on the crystal field spectra of Fe^{3+} in minerals. Lunar Planet. Sci. 14, 692–693 (abstract).

Sherman, D.M., Vergo, N., 1988. Optical (diffuse reflectance) and Mössbauer spectroscopic studies of nontronite and related Fe-bearing smectites. Am. Mineral. 73, 1346–1354.

Sherman, D.M., Waite, T.D., 1985. Electronic spectra of Fe^{3+} oxides and oxide hydroxides in the near IR to near UV. Am. Mineral. 70, 1262–1269.

Shkuratov, Yu.G., Akimov, L.A., Vokhmentzev, A.Ya., Antipova-Karataeva, I.I., 1985. An optical study of carbonaceous chondrites and basalt achondrites. Lunar Planet. Sci. 16, 777–778 (abstract).

Smith, G., 1978. A reassessment of the role of iron in the 5,000–30,000 cm^{-1} region of the electronic absorption spectra of tourmaline. Phys. Chem. Miner. 3, 343–373.

Smith, H.G., Langer, K., 1982. Single crystal spectra of olivines in the range 40,000–5,000 cm^{-1} at pressures up to 200 kbar. Am. Mineral. 67, 343–348.

Soshea, R.W., Dekker, A.J., Sturtz, J.P., 1958. X-ray induced color centers in MgO. J. Phys. Chem. Solids 5, 23–33.

Sprague, A.L., Roush, T.L., 1998. Comparison of laboratory emission spectra and Mercury telescopic data. Icarus 133, 174–183.

Sprague, A.L., Hunten, D.M., Lodders, K., 1995. Sulfur at Mercury, elemental at the poles and sulfides in the regolith. Icarus 118, 211–215.

Sprague, A.L., Emery, J.P., Donaldson, K.L., Russell, R.W., Lynch, D.K., Mazuk, A.L., 2002. Mercury: Mid-infrared (3–13.5 μm) observations showing heterogeneous composition, presence of intermediate and basic soil types, and pyroxene. Meteorit. Planet. Sci. 37, 1255–1268.

Stair, R., Johnson, R., 1953. Ultraviolet spectral radiant energy reflected from the Moon. J. Res. Nat. Bur. Stand. 51, 81–84.

Stanin, F.T., Taylor, L.A., 1979. Armalcolite/ilmenite: Mineral chemistry, paragenesis, and origin of textures. Proc. Lunar Sci. Conf. 10, 383–405.

Strens, R.G.J., Wood, B.J., 1979. Diffuse reflectance spectra and optical properties of some iron and titanium oxides and hydroxides. Mineral. Mag. 43, 347–354.

Tossell, J.A., 1979. Oxygen–metal charge transfer energies in minerals. Lunar Planet. Sci. 10, 1236–1238 (abstract).

Tossell, J.A., Vaughan, D.J., Johnson, K.H., 1974. The electronic structure of rutile, wustite, and hematite from molecular orbital calculations. Am. Mineral. 59, 319–334.

Ullrich, K., Langer, K., Becker, K.D., 2002. Temperature dependence of the polarized electronic absorption spectra of olivines. Part 1. Fayalite. Phys. Chem. Miner. 29, 409–419.

Vilas, F., Hendrix, A.R., 2006. Space weathering on asteroids: New results from the ultraviolet. Lunar Planet. Sci. 37. Abstract 2447 [CD ROM].

Vilas, F., Sprague, A.L., Izenberg, N.R., McClintock, W.E., Domingue, D.L., Holsclaw, G.M., Bradley, E.T., Blewett, D.T., Robinson, M.S., Kochte, M.C., Lankton, M.R., Murchie, S.L., Donaldson Hanna, K.L., Jensen, E.A., 2008. Ultraviolet reflectance spectra of Mercury's surface acquired with the ultraviolet and visible spectrometer during the first MESSENGER flyby. Lunar Planet. Sci. 39. Abstract 1212 [CD ROM].

Wagner, J.K., 1980. Reflection spectroscopy of stony meteorites in the vacuum ultraviolet spectral region. Ph.D. dissertation, Univ. Pittsburgh, Pittsburgh, PA, 215 pp.

Wagner, J.K., Cohen, A.J., Hapke, B.W., Partlow, W.D., 1979. Vacuum ultraviolet reflectance spectra of group H chondrites. Proc. Lunar Sci. Conf. 10, 1797–1818.

Wagner, J.K., Cohen, A.J., Hapke, B.W., Partlow, W.D., 1980. Vacuum ultraviolet reflectance spectra of groups L, LL, and E chondrites and of achondrites. Proc. Lunar Sci. Conf. 10, 775–797.

Wagner, J.K., Hapke, B.W., Wells, E.N., 1987. Atlas of reflectance spectra of terrestrial, lunar, and meteoritic powders and frosts from 92 to 1800 nm. Icarus 69, 14–28.

Warell, J., 2003. Properties of the Hermean regolith. III. Disk-resolved vis-NIR reflectance spectra and implications for the abundance of iron. Icarus 161, 199–222.

Warell, J., Blewett, D.T., 2004. Properties of the Hermean regolith. V. New optical reflectance spectra, comparison with lunar anorthosites, and mineralogical modelling. Icarus 168, 257–276.

Warell, J., Sprague, A.L., Emery, J.P., Kozlowski, R.W.H., Long, A., 2006. The 0.7–5.3 μm IR spectra of Mercury and the Moon: Evidence for high-Ca clinopyroxene on Mercury. Icarus 180, 281–291.

Weidner, V.R., Hsia, J.J., 1981. Reflection properties of pressed polytetrafluoroethylene powder. J. Opt. Soc. Am. 71, 856–861.